2018-12-01

Examining the Mechanics Responsible for Strain Delocalization in Metallic Glass Matrix Composites

Casey Owen Messick
Brigham Young University

Examining the Mechanics Responsible for Strain Delocalization in Metallic Glass Matrix Composites

Casey Owen Messick

A thesis submitted to the faculty of
Brigham Young University
in partial fulfillment of the requirements for the degree of

Master of Science

Eric R. Homer, Chair
David T. Fullwood
Oliver K. Johnson

Department of Mechanical Engineering

Brigham Young University

ABSTRACT

Examining the Mechanics Responsible for Strain Delocalization
in Metallic Glass Matrix Composites

Casey Owen Messick
Department of Mechanical Engineering, BYU
Master of Science

Metallic glass matrix composites (MGMCs) have been developed to improve upon the ductility of monolithic metallic glass. These composites utilize a secondary crystalline phase that is grown into an amorphous matrix as isolated dendritic trees. This work seeks to understand the mechanisms underlying strain delocalization in MGMCs in order to better direct efforts for continual progress in this class of material. A mesoscale modelling technique based on shear transformation zone (STZ) dynamics is used to do so. STZ dynamics is a coarse grained technique that can provide insight into the microscopic processes that control macroscopic behavior, but which can be difficult to resolve experimentally.

A combined simulated-experimental approach to extract the individual material properties of the amorphous and crystalline phases is presented. Numerically, STZ dynamics is used to simulate nanoindentation of the crystalline and amorphous phases respectively. The indented phases are modelled as discs with varying thickness embedded in the other phase. Indentation depths are held constant. Experimentally, nanoindentation is carried out on DH2 and DH3 MGMC composites under varying loads at Stony Brook University (SBU). Specimens are cross-sectioned and using scanning electron microscopy, indentation sites are chosen so that the indenter targets individual phases. For both experimental and simulated nanoindentation, hardness and modulus values are calculated from the load-displacement data. The experimental and simulated values are normalized and compared. Good agreement between results suggests accurate characterization of the individual phases at low loads on both DH2 and DH3 composites. Length scales at which indentations begin sampling outside the intended phase are presented.

Work is then presented on simulated uniaxial tensile loading of MGMCs. Dendritic microstructural sizes are varied and shear banding characteristics are measured. A competition of shear band nucleation and propagation rates that previously had only been seen in monolithic metallic glasses under certain loading conditions is found to exist in MGMCs as well. The stages of shear banding in MGMCs are presented and the influence of dendrites on shear band nucleation and propagation are discussed. It is proposed that the introduction of dendrites into the amorphous matrix work to inhibit shear band propagation and encourage shear band nucleation to delocalize strain in MGMCs. In particular, it was found that smaller dendrite sizes and spacings are better at doing so.

Keywords: shear transformation zone, shear band, metallic glass, metallic glass matrix composites, competition of rates, strain delocalization, STZ dynamics

ACKNOWLEDGEMENTS

Many thanks to Eric Homer for his trust in me and for his guidance and to my wife Sabrina for her long suffering and support through many late and lonely nights. I would like to acknowledge work on experimental nanoindentation of the metallic glass matrix composites presented here was conducted by Jonathan Gentile at Stony Brook University under the direction of Jason Trelewicz.

This work was funded by the National Science Foundation under Contract No. CMMI-1401777. Any opinions, findings, and conclusions or recommendations expressed in this material are those of the author(s) and do not necessarily reflect the views of the National Science Foundation.

TABLE OF CONTENTS

LIST OF TABLES

LIST OF FIGURES

1 INTRODUCTION

1.1 Bulk metallic glass

Designing materials that have an impressive array of mechanical characteristics, such as strength, toughness, elasticity, and ductile failure, has driven the research work of many materials scientists. The study and development of bulk metallic glasses (BMGs) is a classic representation of this endeavor. The first metallic glass was produced by Duwez and coworkers in 1960 [1]. By cooling a liquid melt at sufficiently high rates ($\sim 10^6$ K s^{-1}) they succeeded in bypassing crystalline nucleation resulting in an amorphous metallic alloy. These alloys could only be fabricated as thin ribbons due to the necessarily high cooling rates. In the early 1990s however, new La-, Mg-, and Zr-based amorphous structures that could be created using lower cooling rates allowed the formation of the first BMGs of up to 1cm in size [1]–[5]. These advances resulted in the ability to investigate the structural and mechanical properties of these glassy metals at the macro-scale.

By successfully retaining their amorphous atomic structure in solid state, BMGs demonstrate drastically improved yield strengths over their crystalline counterparts. This is attributed to their lack of long range order which negates mechanisms, such as dislocations, common in crystalline metals. BMGs also have high elastic limits, that when combined with their high strengths place BMGs in unique material property spaces not before attainable with traditional materials [6]–[9]. This is demonstrated in Figure 1-1 where the elastic and strength properties are displayed on an Ashby type plot.

An amorphous atomic structure also results in low shrinkage rates. Combined with viscous flow at high temperatures, metallic glasses are able to undergo thermoplastic polymer and conventional glass forming processes. This provides incredible flexibility in shaping metallic glass with micro scale precision and eliminating the need for expensive secondary finishing processes (injection molding, superplastic extension and extrusion, and blow molding for example) [9]–[12]. Because of these and other traits, BMGs have been hailed as the material of the future since the 1960s [1], [3]–[5], [9], [13]. Despite their accolades, metallic glasses have not seen widespread adoption into small-scale structural applications. This is largely a result of their tendency to fail catastrophically upon yield.

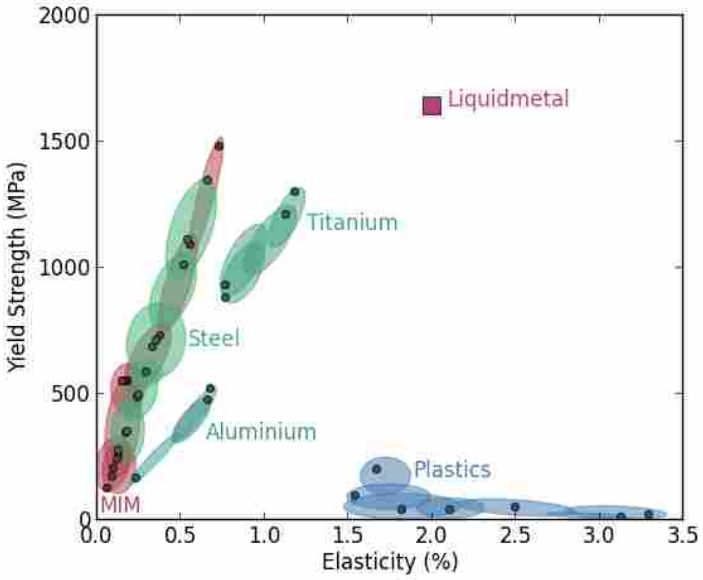

Figure 1-1: Ashby type chart
Demonstrating the superiority of combined strength and elasticity in metallic glasses over other material classes (used with permission from LiquidMetal Technologies).

1.1.1 Shear localization in metallic glass

The reason why BMGs fail catastrophically upon yield is attributed to the rapid growth and development of shear bands. Shear bands develop from the accumulation of many local

rearrangements in the atomic structure due to applied stresses [14]. Unlike crystalline metals that often demonstrate a variety of microscale deformation mechanisms (dislocations, twinning, grain boundary sliding…etc.), the deformation of metallic glass is governed primarily by one mechanism [15]–[17]. One such explanation of this mechanism has been termed a shear transformation zone (STZ).

An operation or activation of an STZ is described as a cluster of atoms that undergoes shear distortion to accommodate strain. Although the collective activation of many STZs can vary depending on loading condition, under normal loading rates and temperatures, STZ activations tend to form into STZ clusters that then form into unstable shear bands. Under unconstrained modes of loading, further accumulation of strain is concentrated in one to a few shear bands, resulting in fracture. This entire process is seen to occur over periods of 10^{-5}-10^{-3} s in experiments [18]–[21].

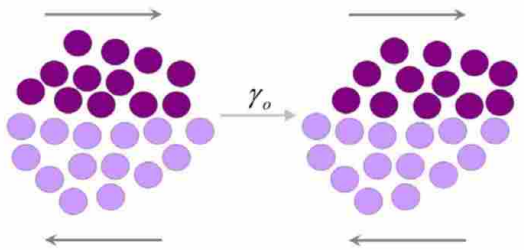

Figure 1-2: Two dimensional schematic depicting an STZ proposed by Argon [15]
Figure taken from [22].

Despite the tendency for metallic glass to fail catastrophically, a unique and encouraging observation can be seen. The individual accommodation of strain by a single shear band can be on the order of 100% or more and demonstrates incredible local ductility. Because strain is usually concentrated in only a few shear bands that develop quickly, there is little to no

detectable strain at the macroscopic level [23]. It then follows that if a greater number of shear bands would form, macroscopic plasticity could improve. In recent work, this has been demonstrated in two ways: 1) Deformation of metallic glass at high strain rates and 2) the introduction of a secondary crystalline phase into the amorphous matrix.

1.1.2 Rate dependence in metallic glass

As previously introduced, when metallic glasses are deformed, fracture will rapidly develop along a few runaway shear bands [14], [24]–[29]. In contrast, when deformed at higher strain rates, a higher number of fracture planes corresponding with an increased number of runaway shear bands are seen. Accompanied increases in macroscopic plasticity is also evident from stress-strain curves (Figure 1-3) [25]–[29].

Figure 1-3: True stress-strain curves for Vitreloy 1
Data shown is from tensile tests at different strain rates [27]

Figure 1-4: Nanoindentation of Vitreloy-105
Indentations at different loading rates from **[30]**. Inset showing SEM micrograph of shear banding steps from a nanoindentation site.

This flow transition has also been demonstrated in experimental nanoindentation. Due to constrained modes of loading under nanoindentation, when metallic glasses are indented, they produce a distinctly serrated load-displacement curve. The serration points correspond with displacement bursts from propagating shear bands [31]–[34]. As metallic glasses are indented at higher rates, serrations become smaller and smaller until they are virtually non-existent (Figure 1-4 [30]). Schuh et al. employed nanoindentation to more fully quantify flow regimes as a function or rate and temperature populating a deformation map shown in Figure 1-5. For the transition from strong to medium to light flow serration at lower temperatures, Schuh et al. hypothesized that this was a result of a change from a few to many shear bands as a result of a competition between shear band nucleation and propagation rates. As the strain rate surpasses an

intrinsic shear banding frequency, shear bands are able to nucleate but unable to propagate fast enough to relax the material sufficiently. Consequently, the yield criterion for STZ activation and shear band nucleation is still widely met throughout the specimen encouraging STZs to activate in a homogeneous manner. In other words, more shear bands enter the nucleation stage but fewer enter the propagation stage resulting in the increased and simultaneous operation of many shear bands [35]–[38].

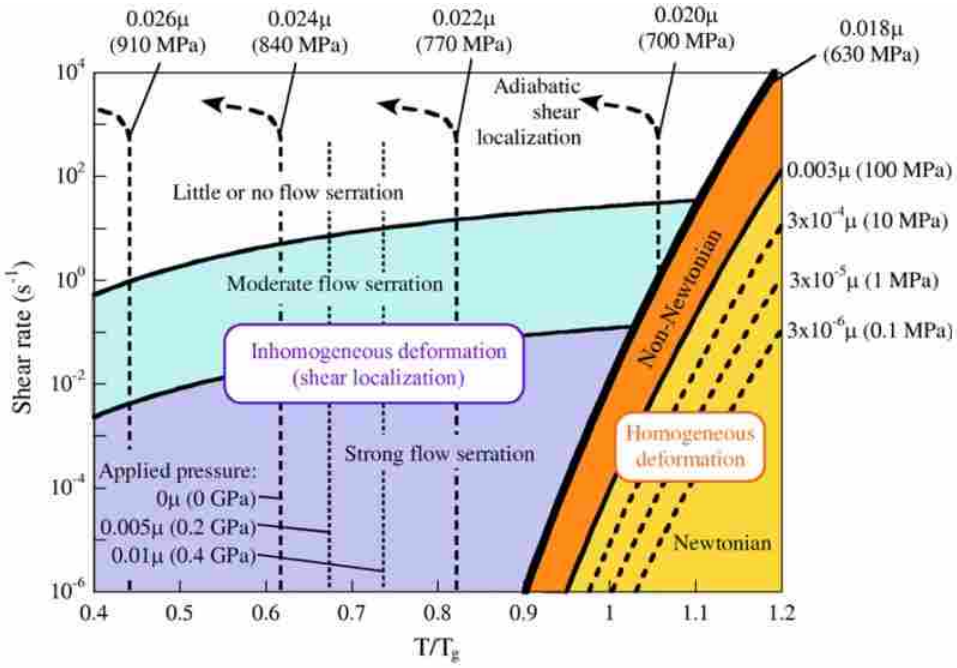

Figure 1-5: Strain rate-temperature deformation map for metallic glass
Taken from a review article by Schuh et al. [14]. Homogenous and inhomogeneous flow is separated by the thick solid line.

This hypothesis was corroborated in a recent work by Harris et al. [39]. Using shear transformation zone (STZ) dynamics, they were able to numerically simulate the deformation of metallic glass at varying strain rates. The magnitude of flow serration in the simulation appeared to show transitions from strong to medium and medium to lightly serrated flow at the same rates predicted by nanoindentation experiments carried out by Schuh et al. [35]. Not only this, but

analysis of shear banding characteristics demonstrated that accompanying the transition from strongly serrated flow (low strain rates) to lightly serrated flow (high strain rates) was an increase of shear band nucleation rates and a decrease in shear band propagation rates. They were able to verify the hypothesis in [35] that at lower strain rates, shear bands nucleate and propagate quickly to allow stress to reduce in the surrounding material; but at high strains rates, strain is not accommodated quickly enough to relieve stress resulting in the simultaneous operation of shear bands throughout the specimen.

1.2 Metallic glass matrix composites

1.2.1 Increased shear banding in metallic glass matrix composites

Another way that strain has been effectively delocalized in amorphous metals has been with the development of MGMCs [40]–[42]. These composites utilize a secondary crystalline phase that is grown into the matrix as isolated dendritic trees [42]–[46]. They have demonstrated more than 10% strain under biaxial tensile loads with strengths as high as 1.5 GPa. Their high strengths combined with tensile ductility make them very attractive for applications where high toughness is needed [46]–[51].

As already mentioned, when metallic glasses are plastically deformed at conventional loading rates, they fail along a fairly defined shear plane and show little, if any, overall plasticity. However, when MGMCs are deformed, strain is delocalized through the proliferation of shear bands throughout the specimen. This is commonly evidenced by an undefined shear plane signifying numerous runaway shear bands seen on fracture surfaces under uniaxial loading conditions (Figure 1-6) [48], [52].

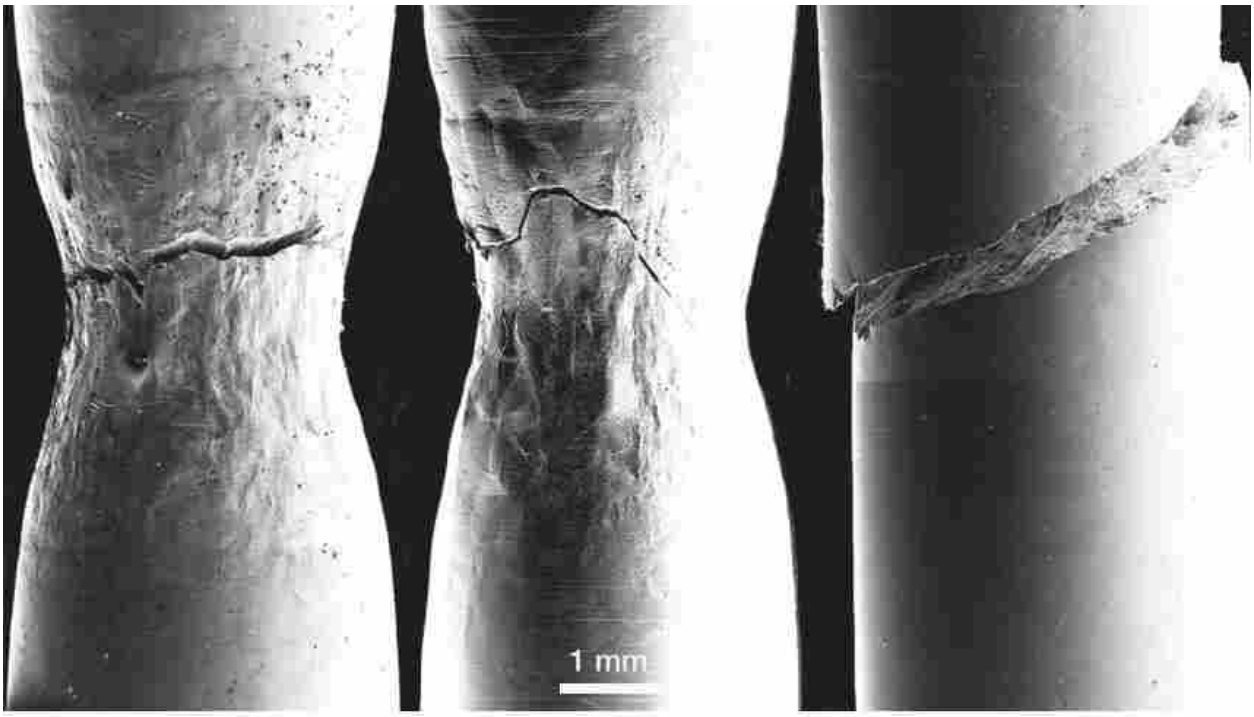

Figure 1-6: SEM micrograph of the tensile surfaces of DH2, DH3, and a monolithic BMG (listed left to right) [46]

Notably, the development of DH1, DH2, and DH3 zirconium based MGMCs by Hofmann et al. [53] has seen particular success [46]–[51], [53]. Microstructural and fractographic analyses revealed matching length scales between shear band sizes and dendrite spacings. Hofmann et al. hypothesized that dendrites can serve to limit shear band propagation to within the domains between the dendrites. If shear band length scales are matched with dendrite spacings, then shear bands are kept from reaching crack initiation sizes and crack development is arrested. As individual shear bands cannot sufficiently relax strain, the simultaneous operation of multiple shear bands is consequently encouraged [53], [54].

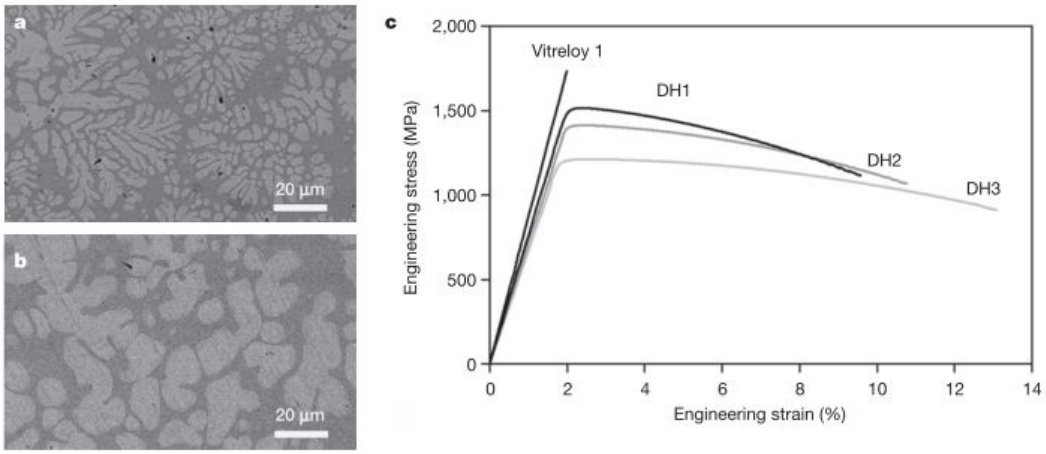

Figure 1-7: Development of DH1, DH2, and DH3
(a) DH1 and (b) DH3 backscattered SEM micrographs illustrating the dendritic structure of the secondary crystalline phase. (c) Engineering stress-strain curves for DH1, DH2, and DH3 at room temperature demonstrates improved tensile ductility when dendrite length scales match shear band sizes Figure taken from [46].

1.2.2 Effects of microstructural features in metallic glass matrix composites

The extent to which the secondary phase can delocalize strain is influenced by some microstructural characteristics including volume fraction, dendrite size, dendrite spacing, and dendrite morphology [44], [46], [49], [55]–[57]. Some efforts to optimize composite design based on the influence of these dendrite features have been documented [44], [50], [58], [59].

First, it is well-known that increasing the volume fraction of the crystalline phase results in significant increases in plasticity. This is most effective when a soft crystalline phase is used, as they are thought to reduce shear band propagation velocities by lowering stresses at the point when shear bands encounter crystalline regions. Despite enhanced plasticity in these cases, it can come at the detriment of decreased composite strength [51], [60]–[66].

Other correlations with dendrite length scales and strain delocalization has also been found [42], [51], [53], [66]–[68]. Some groups have reported that a bimodal distribution of dendrite sizes may be optimal in enhancing plasticity in composites. They theorize that smaller

dendrites lead to an increase in nucleation sites for shear bands, while larger dendrites work more effectively to slow down their propagation [44], [69].

1.3 STZ dynamics

Examining the various stages of shear localization is difficult due to the various time and length scales of these events. STZ activations occur on timescales of about 10^{-12} to 10^{-11} s while shear band formations spans timescales of 10^{-5} to 10^{-3} s [19], [70]. On the other hand, shear band thickness is on the order of 10^{-8} to 10^{-7} m [71], [72], while STZ sizes are on the order of 10^{-10} to 10^{-9} m [47], [73]. STZ dynamics developed by Homer et al. [22] that can span these various time and length scales.

The STZ dynamics model is a mesoscale simulation technique that uses STZs as its fundamental unit of deformation. STZs are modelled as Eshelby inclusions and are coarse-grained onto a finite-element mesh. The activation of STZs is controlled by using a kinetic Monte Carlo (kMC) algorithm [74] and an activation rate law, given by the following:

$$\dot{s} = v_0 \cdot \exp\left(-\frac{\Delta F - \tau \cdot \gamma_0 \cdot \Omega_0}{kT}\right), \tag{1-1}$$

where $\dot{s}$ is the STZ activation rate, ΔF is the activation energy barrier for an STZ activation, τ and T are the local shear stress and temperature in Kelvin respectively, k is the Boltzmann's constant, γ_0 is the incremental shear strain applied to an STZ, Ω_0 is the volume of an STZ, and v_0 is the attempt frequency. The interested reader is directed to [22] for a more detailed explanation of this modelling framework.

1.3.1 Modelling MGMCs using STZ dynamics

The deformation model for a secondary crystalline phase was added to the STZ Dynamics framework by Hardin et al. [75]. The crystalline model follows a ductile plastic constitutive law based on a Taylor dislocation model and the work of Qiao et al. [52] and Zhang et al. [68]. The tensile stress-strain relationship of this model is given by the following:

$$\sigma = \sigma_{ref}\sqrt{\left(\frac{\sigma_y}{E} + \varepsilon^p\right)^{(2n)} + L\bar{\eta}}\,, \tag{1-2}$$

where ε^p is the plastic strain, E is the Young's modulus, σ_y is the yield stress, $\sigma_{ref} = \frac{E^n}{\sigma_y^{n-1}}$, n is the hardening coefficient, $L = 180b\left(\frac{a\mu}{\sigma_{ref}}\right)^2$ is the intrinsic material length where μ, b, and a is the shear modulus, Burgers vector length, and an empirical constant of 0.1 respectively, and $\bar{\eta}$ is the average strain gradient approximated by $\frac{\varepsilon^p}{D}$ where D is a characteristic diameter of the crystalline phase microstructure. The interested reader is directed to [75] for a more detailed explanation.

Hardin et al. [75] added the ability to partition the finite element mesh into two phases to either follow the STZ dynamics deformation model or the Taylor dislocation model. This provides the ability to vary the morphology of the microstructure of the secondary phase and examine its effect on the shear banding process.

1.4 Motivation, aim, and approach

The timeline for including new and novel materials in structural applications is often lengthy and drawn out. Despite the incredible suite of mechanical properties that are already

demonstrated in MGMCs, safety and reliability concerns keep them from being integrated more fully into industry. This research seeks to clarify the underlying mechanism behind strain delocalization in MGMCs.

In particular, it is hypothesized that the competition of rates seen in pure metallic glass at high strain rates also exists and is responsible for strain delocalization in MGMCs. Where high strain rates are the motivating factor for this phenomenon in metallic glass, a secondary dendritic phase can also serve to encourage shear band nucleation by limiting shear band growth. Although some evidence has supported this conclusion, there has been no clear demonstration of rates measurements in MGMCs. This work seeks to validate this hypothesis and provide further insight into the phenomenon behind enhanced ductility in MGMCs.

This research seeks to do so by utilizing STZ dynamics to examine shear banding in MGMCs. Chapter 2 presents a combined simulated-experimental nanoindentation approach for characterization of the individual phases of MGMCs. Chapter 3 utilizes results from nanoindentation experiments and simulations to calibrate model inputs for tensile test simulations of MGMCs. Dendrite length scales are systematically varied to investigate their effects on shear banding characteristics and macroscopic responses. Competition of rates is verified in MGMCs. Correlations between microstructural dendrite length scales and shear banding characteristics are presented.

2 MODELLING THE INFLUENCE OF PROXIMAL PHASES IN NANOINDENTATION OF METALLIC GLASS MATRIX COMPOSITES

2.1 Introduction

2.1.1 Nanoindentation and characterization of individual phases in composites

The extent to how well MGMCs perform are influenced by the individual material properties of its constituents. Although much work has been done to improve properties of these composites, the complex structure of the crystalline dendritic phase make it difficult to unravel the elastic and plastic interactions between the different phases. Continued improvement of these materials will require knowledge of individual phase properties as well as length scales at which the two phases interact. Due to their ability to sample extremely small volumes, nanoindentation can be a useful tool to do obtain this information.

The goal of many nanoindentation tests is to determine the material hardness and Young's modulus from load-displacement data [76]–[80]. For specimens with varying material composition or fine microstructures, this characterization becomes a challenge. In order to accurately capture the material response of one phase, indentation sites must only sample the intended phase. Therefore accurate measurements of individual phases must require sufficiently large regions of indented phases or indentations must be sufficiently shallow so as not to sample the other phases (nanoindentation experiments are on the order of a few microns or hundreds of nanometers [81]).

In order to combat these challenges, shallower indents can be a solution; however, this is not always the appropriate approach as it can introduce new problems [82], [83]. Surface roughness becomes a factor at shallow loads. Polishing effects can also begin to skew measurements. Without *a priori* knowledge of the elastic and plastic zone sizes, it is difficult to confirm if the calculated material properties truly reflect the indented phase using nanoindentation experimentation alone.

2.1.2 Combined simulated-experimental approach to determine properties of the individual phases of composites

A combined simulated-experimental approach can be used effectively to verify material properties calculated by indentation. Experimental nanoindentation can provide data points to either validate or deny using numerical simulations. Numerical simulations can be adapted and fitting parameters can be adjusted to determine the closest representative material properties.

Numerical simulations has be useful in understanding the mechanics behind composite nanoindentation [84]–[90]. Yan et al. [91], [92] conducted a finite element analysis on the nanoindentation of elastic spherical particles embedded in an elastic matrix. They reported numerous values denoted by "particle-dominated depth" beyond which the matrix will influence the apparent elastic properties of the particle. Durst et al. [86] also demonstrated the simulated nanoindentation of a particle-matrix system but examined depth limits for hardness. They similarly reported a transition from particle to matrix deformation behavior during indentation and concluded that particle hardness can be reliably tested up to normalized contact radius of about 70% particle diameter.

STZ dynamics was previously used to simulate case of indentation loading [74]. However, the work presented was not appropriate for a quantitative comparison with experimental nanoindentation. The main reasons being the use of plane strain elements (the indenter is assumed to be an infinitely long cylinder indenting an infinitely thick out of plane specimen) and differing material properties. In the present work, a combined simulated-experimental approach is used to verify material properties of the individual phases in MGMCs. Insight is also shared as to the length scales on which the two phases interact.

2.2 Method

A combined simulated-experimental approach is utilized to calculate individual phase properties in Zirconium based MGMCs [53]. Numerical simulations are run at Brigham Young University using STZ dynamics and nanoindentation experiments are carried out at Stony Brook University (SBU) by Jonathan Gentile, under the direction of Jason Trelewicz, on DH2 and DH3 composites [46]. All measurements on experimental nanoindentation presented here was provided by SBU. This section first details the process used to measure nanoindentation load-displacement data experimentally. Next, the modelling framework for using STZ dynamics to simulate nanoindentation of MGMCs is described. Finally, the method used to convert both the numerical and experimental data into hardness and modulus properties is explained.

2.2.1 Experimental nanoindentation of DH2 and DH3 composites

2.2.1.1 Procedure

To obtain individual phase properties, nanoindentation tests are carried out on DH2 and DH3 composites at SBU (DH1 dendrite sizes and spacings were too small to be able to comfortably locate the indenter entirely in one phase). Scanning electron microscopy (SEM),

images in Figure 2-1 show targeted indentation of the individual phases. Indentations are carried out for both DH2 and DH3 at the following loads: 2mN, 3mN, 4mN, 5mN, 7.5mN, and 10mN. At each load, roughly 3 sets of indentations were conducted (see Figure 2-1 for an example of one set). After the indentations were completed, hardness and elastic modulus values were calculated using conventional methods described in the Section 2.2.2 below.

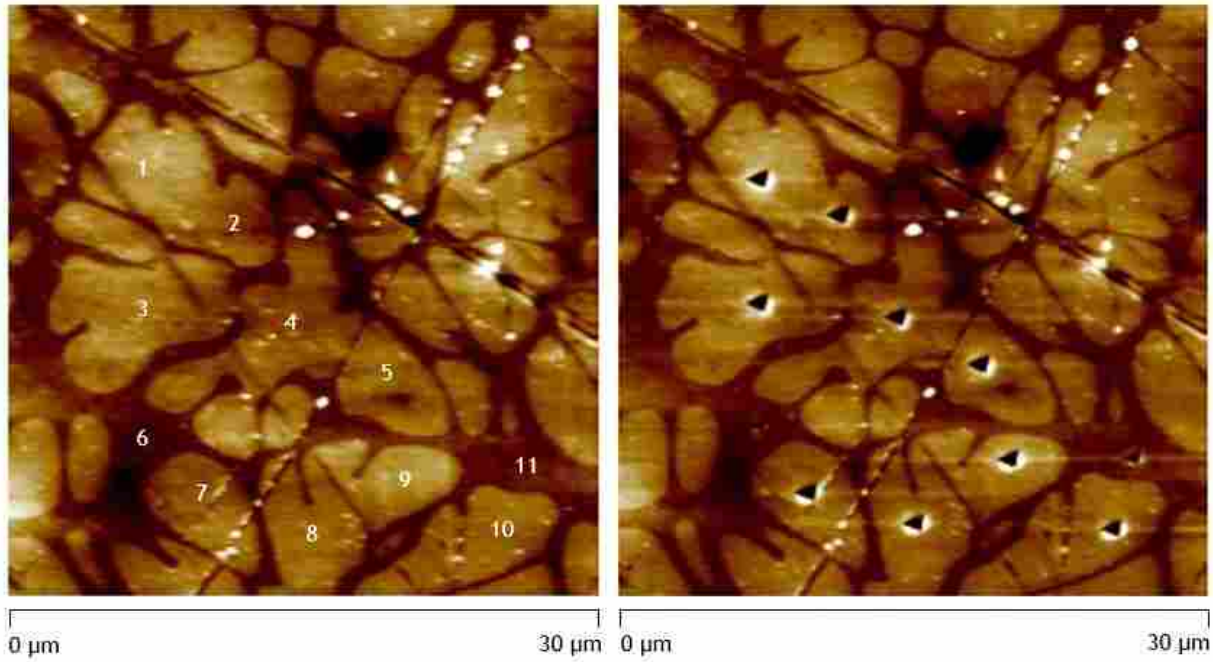

Figure 2-1: Indentation of the crystalline phase in DH3 at 2mN indentation load

2.2.2 Simulating nanoindentation of MGMCs using STZ dynamics

2.2.2.1 STZ dynamics modelling framework

2.2.2.1.1 Element type

For quantitative comparison of numerical simulations with experimental data, the STZ dynamics model is modified to allow the use of axisymmetric elements (CAX6MT) in place of

plain strain elements (CPE6MT). This allows the model to more accurately capture the boundary conditions and mechanics seen in experiments.

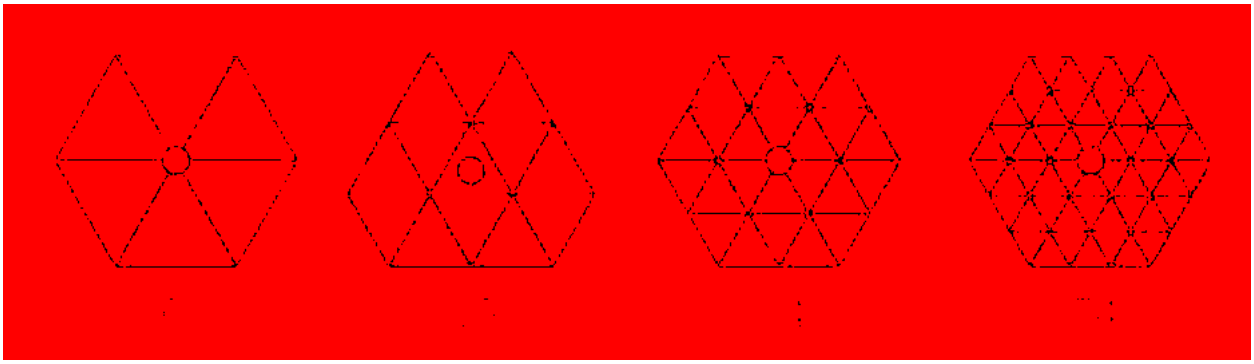

Figure 2-2: Representation of several possible STZ definitions in the finite element mesh. The group of 24 elements is utilized in this work.

2.2.2.1.2 Mesh refinement

The STZ dynamics model is also adapted to utilize a denser mesh to account for the complex stress state in these simulations. Optimally, the mesh would have been refined directly beneath the indenter tip and coarsened gradually as the elements are further form the indentation site. However, in order to model STZs accurately, STZs are coarse-grained as a group of elements that together approximate the shape of a circle. In order to keep STZ volumes consistent, element size must remain consistent throughout the finite element mesh. In this work, the center of STZs are represented by any corner node of an element. Two rows of elements extending radially outward will participate in the STZ activation (or a group of 24 elements as denoted in Figure 2-2). This allows the use of an appropriately refined mesh while keeping computation burdens manageable. It was found that using the configuration denoted by 54 (meaning 54 elements) in Figure 2-2 did not yield significantly improved indentation responses suggesting convergence of the mesh with 24 elements.

2.2.2.1.3 Boundary conditions

The simulation specimens are modelled as a cylinder 120nm tall with a radius of 70nm. These sizes are limited by computational constraints. The bottom edge of the cell is fixed and an axisymmetric boundary condition is applied to the wall coincident with the y-axis. This allows elements touching this wall to displace vertically but keeps nodes from crossing over the axis. For the indentations in this work, it was found that there was no significant interaction of the stress field with the boundaries at these sizes.

2.2.2.1.4 Indentation conditions

In the axisymmetric model, the indenter is located above the axis of revolution, which is defined as the far left wall as shown in Figure 2-4. The indenter is modelled as a rigid surface. A 70.3° half-angle conical indenter is employed which has the same contact area-to-contact depth ratio as a Berkovich tip and is commonly used in 2D simulations [93], [94]. A friction coefficient of 0.05 is applied to the contacting surfaces between the indenter and the specimen [95].

A constant displacement rate is used to achieve a strain rate of roughly $10\ s^{-1}$. While experimentally, the loading rate is held constant and the displacement rate is allowed to vary, in this work, it was found to yield no difference in numerically measured values if displacement or loading rates were held constant. As such, a constant displacement rate of 0.1 nm/s is used in this work in order to match average rates seen in nanoindentation experiments. Additionally, it is worth noting that measured material properties were not sensitive to differences in displacement rates.

2.2.2.2 STZ dynamics model inputs

In an effort to match the properties of the DH2 and DH3 composites tested experimentally, the model uses independent properties for the amorphous and crystalline phases. Values for these properties are taken from the literature where possible.

The crystalline phase is modeled with a yield strength of 850 MPa, a Young's modulus of 90.5 GPa, and a strain hardening exponent of 0.2 are used. These values are chosen as the yield strength is comparable to estimated yield strength values reported by Hofmann et al [53] and to calculated yield strengths from different material models [96], [97].

For the amorphous phase we use a slightly adjusted model provided by Harris et al. [39] to calculate the material and geometric STZ properties. This model is required to account for strain rate dependent yield strength when using STZ dynamics. To achieve the yield strength of 2.1 GPa (common to monolithic metallic glasses [98]) at a strain rate of 10 s^{-1}, Harris's adjusted model requires an STZ volume of 1.8 nm^3 and an activation energy barrier of 1.535 eV is used. This was verified with a uniaxial tensile loaded simulation. Additional properties for the metallic glass phase used a shear modulus of 39.94 GPa, a Poisson's ratio of 0.352, and a Debye temperature of 327 K [22].

All required inputs for the two phases are summarized in Table 2-1 and characteristic indentation load-displacement curves for the amorphous and crystalline phases are shown in Figure 2-3. Initial simulated and experimental load-displacement data yielded similar curves indicating valid inputs.

Table 2-1: Model parameters for the amorphous and crystalline phases

Property	Symbol & value
Amorphous parameters	
Shear modulus	μ = 39.94 GPa
Poisson's ratio	ν = 0.352
Debye temperature	327 K
Activation energy barrier	ΔF = 1.535 eV
STZ shear strain	γ_0 = 0.1
STZ volume	Ω_0 = 1.8 nm^3
Crystalline parameters	
Shear modulus	μ = 34.02 GPa
Poisson's ratio	ν = 0.33
Yield stress	σ_{ys} = 850 MPa
Microstructure length	D = 50 nm
Burger's Vector	b = 2.858 Å
Empirical constant	a = 0.1
Hardening coefficient	n = 0.2

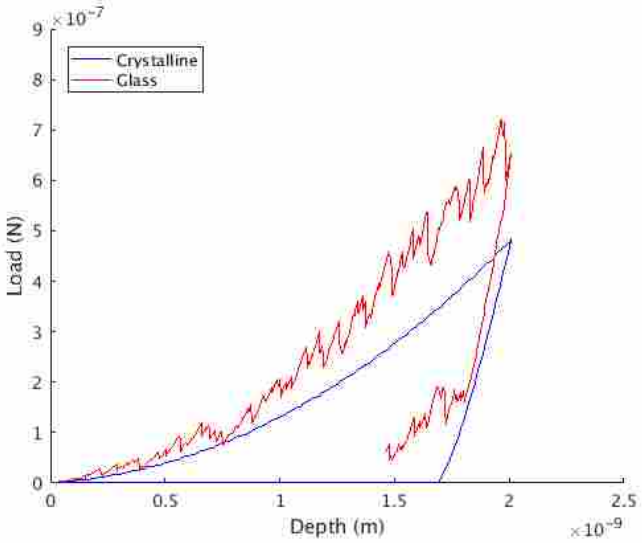

Figure 2-3: Load-displacement curves for the amorphous and crystalline phases. Simulations created using material inputs shown in Table 2-1.

2.2.2.3 Procedure

Indentations are carried out on the crystalline and amorphous phases and load-displacement data is measured. To understand the influence of the size of the region being indented and its proximity to neighboring phases, the indented phase is modelled as a disc of one phase with varying thickness embedded in a matrix of the other phase. The thickness of the indented disc, *t*, is varied while the indentation depth, *h*, is held constant such that the normalized indentation depth (*h/t*) ranges from 2% to 90% (see Figure 2-4). The max indentation depth, *h*, is fixed at 2 nm for all simulations.

Due to the stochastic nature of the STZ dynamics, indentations of the glass phase required an average of 3 simulations to estimate the hardness and Young's modulus properties. This is unnecessary for the crystalline material model because its lack of stochasticity results in identical load displacement curves in each simulation.

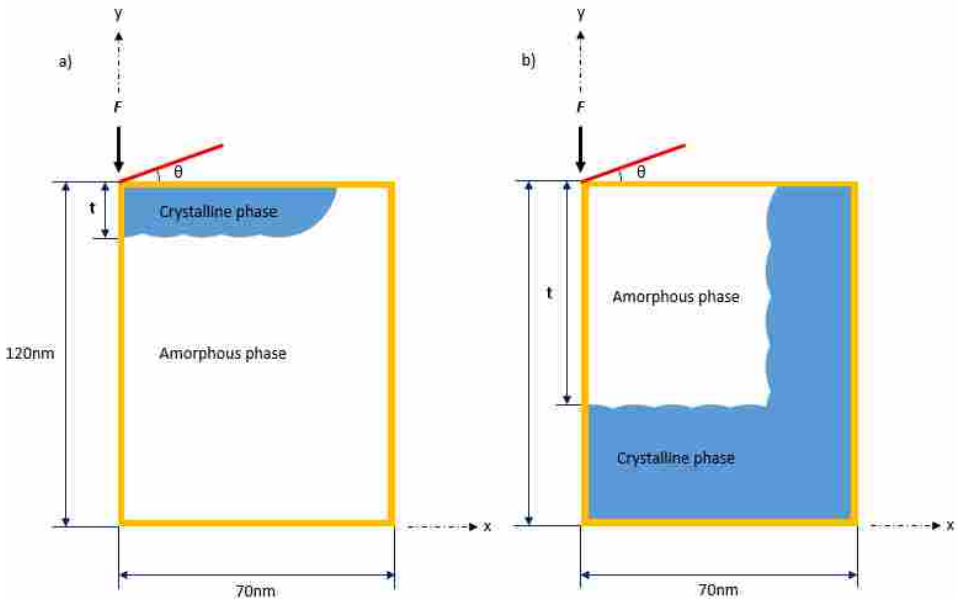

Figure 2-4: Schematic illustration of simulated nanoindentation.
a) Indentation of the crystalline phase and b) indentation of the matrix both with varying thickness, 't'.

After all the simulations are run, material hardness and elastic modulus is calculated using load-displacement data as described in Section 2.2.2 immediately following.

2.2.3 Conventional method to calculate hardness and modulus of the indented phase

For both the experimental and simulated nanoindentation, the hardness and elastic modulus are calculated using conventional methods established by [80], which are explained here.

Hardness is measured as a ratio of the maximum indentation load and the contact area at maximum depth [80]:

$$H = \frac{P_{max}}{A} \tag{2-1}$$

where P_{max} is the maximum indentation load and A is the projected contact area at maximum depth.

The modulus is measured by the relationship between contact area and the measured unloading stiffness, given as,

$$S = \beta \frac{2}{\pi} E_r \sqrt{A} \tag{2-2}$$

where E_r is the reduced elastic modulus defined by,

$$\frac{1}{E_r} = \frac{1-\nu^2}{E} + \frac{1-{\nu_i}^2}{E_i} \tag{2-3}$$

where E and v is the modulus and Poisson's ratio for the specimen and indenter (denoted with no subscript and the subscript i, respectively) and β is the correction factor. A value of 1.025 for β is used in this work [80]. The stiffness, S, is calculated by fitting the unloading portion of the indentation graph data to the following power-law relation:

$$P = B(h - h_f)^m \,, \tag{2-4}$$

where B and m are fitting parameters, P is the indentation load, and h is the indentation depth with h_f being the residual indentation depth after unloading. The contact stiffness is then determined by differentiating Eq. (2-4) and evaluating at the maximum depth, h_{max}. This yields the following equation:

$$S = Bm(h_{max} - h_f)^{m-1} \,, \tag{2-5}$$

In the numerical simulations, displacement bursts from high levels of STZ activation in the amorphous phase and the small scale of the simulations lead to load-displacement data that is noisy. To combat sensitivity of these calculations the data used for fitting parameters only uses between 5% and 80% of the unloading portion of the load-displacement curve. This was not done for the experimental data.

2.3 Results

2.3.1 Hardness and Modulus measurements

Hardness and modulus values are calculated from the load displacement data using the method described in Section 2.2.2. These values are shown in Figure 2-5. Subsets a) through d) show experimental modulus and hardness values as a function of maximum indentation load.

DH3 and DH2 measurements are shown on plots separate from each other for ease of interpretation. The blue and orange dots show average hardness and modulus values as measured when the crystalline phase and the amorphous phase was targeted respectively at each indentation load. The yellow and grey lines represent chosen reference hardness and modulus values for the amorphous and crystalline phases respectively. The measured values for the DH3 specimens at their lightest load are chosen as reference values, which would be expected to be representative of the individual phases. They allow ease of viewing deviations as indentation load is varied. For reference, as indentation loads are increased, the indenter is pushed further into the specimen. This can be compared to indenting a thinner phase. As such, the values from left to right can be approximated as indenting a phase that gets progressively thinner. Subsets e) and f) show modulus and hardness values as measured numerically as a function of normalized indentation depth, h/t (thick to thin from left to right). The yellow and grey lines represent the calculated hardness and modulus values for the amorphous and crystalline phases respectively if the specimen consisted entirely of one phase or the other. Again, this is useful to examine deviations as normalized indentation depth increases.

2.3.2 Influence of the underlying phase

The measured hardness and modulus values for DH3 specimens do not begin to sample the underlying substrate as early as it does in the DH2 specimens. This can be attributed to smaller dendrites and spacings found in DH2 MGMCs. The indentations to the same depth will, on average, penetrate a greater portion of the indented phase in the DH2 than the DH3 specimens. This means that the underlying substrate will begin to influence measured material properties at much lower indentation loads.

For experimental results, as indentation loads get higher, we see a convergence of material properties towards the softer phase. This is most clearly seen with measurements in the DH2 phase. In contrast, simulated results do not demonstrate this same effect. As the indented phase gets thinner, values begin to simply reflect more of the underlying phase. This is likely because the experimental microstructure is much more complex than what has been simulated here.

For numerical measurements of the elastic modulus, the measured values can be visibly seen from Figure 2-5(e) to almost immediately begin to deviate as the indented phase gets thinner or the indenter is pushed deeper. Despite an obvious influence of the underlying substrate, this influence is slightly exaggerated on the scale shown in Figure 2-5(e). When the percent error is calculated for the simulated nanoindentation, there is in fact very little deviation from the known value. Even when indented 15% into the phase, the deviation of the measured to actual modulus values are less than 1% for the glass phase and less than 5% for the crystalline phase (see Table 2-2). At the very deepest normalized indentations, the percent deviation is still less than 15%.

On the other hand, at first glance, numerically measured hardness values look to be fairly consistent till about indentation of about 20% into the intended phase. This is to be expected because hardness is related to plasticity which has a much smaller field. This is verified by looking at the percent deviation from known inputs. At 20% indentation, we see hardness values still very close to the known input. However, after this inflection point, percent deviation begins to increase quickly. In fact, at just 31% indentation, there is over 15% error in measured values. See Table 2-2 for greater detail on the percent deviations.

It seems that although modulus values begin to deviate earlier, they see less of an influence from the secondary phase at deeper indentations than hardness. On the other hand, hardness values deviate later, and once they begin to see the influence of the secondary phase, the values are drastically compromised. Because hardness measurements are plastic and more localized in nature, once it begins to sample the secondary phase, a large portion of the plastic field will quickly be consumed by the secondary phase. On the other hand, modulus measurements are elastic in nature and much less localized. Therefore, despite the indenter getting fairly close to the secondary phase, the elastic field still samples a large portion of the indented phase and the secondary phase fails to dominate to as large a degree when compared with hardness.

Table 2-2: Percent error of measured values against known model inputs.

	Percent Error			
h/t (%)	E (crystalline)	H (crystalline)	E (glass)	H (glass)
2%	0.25%	2.43%	0.94%	0.49%
3%	0.48%	2.39%	2.85%	0.73%
3%	0.81%	2.34%	2.58%	2.89%
5%	1.60%	2.24%	0.64%	1.28%
8%	2.54%	2.12%	0.07%	1.38%
10%	3.33%	2.00%	0.91%	2.71%
13%	4.19%	1.85%	0.52%	0.52%
14%	4.21%	1.69%	0.50%	0.87%
20%	6.80%	0.19%	2.23%	5.98%
31%	10.10%	7.02%	3.40%	15.89%
40%	7.32%	4.31%	5.72%	31.16%
50%	8.94%	8.80%	6.39%	23.85%
67%	10.94%	13.99%	5.20%	33.27%
80%	12.31%	18.31%	7.33%	35.75%
90%	15.29%	25.71%	9.96%	26.25%

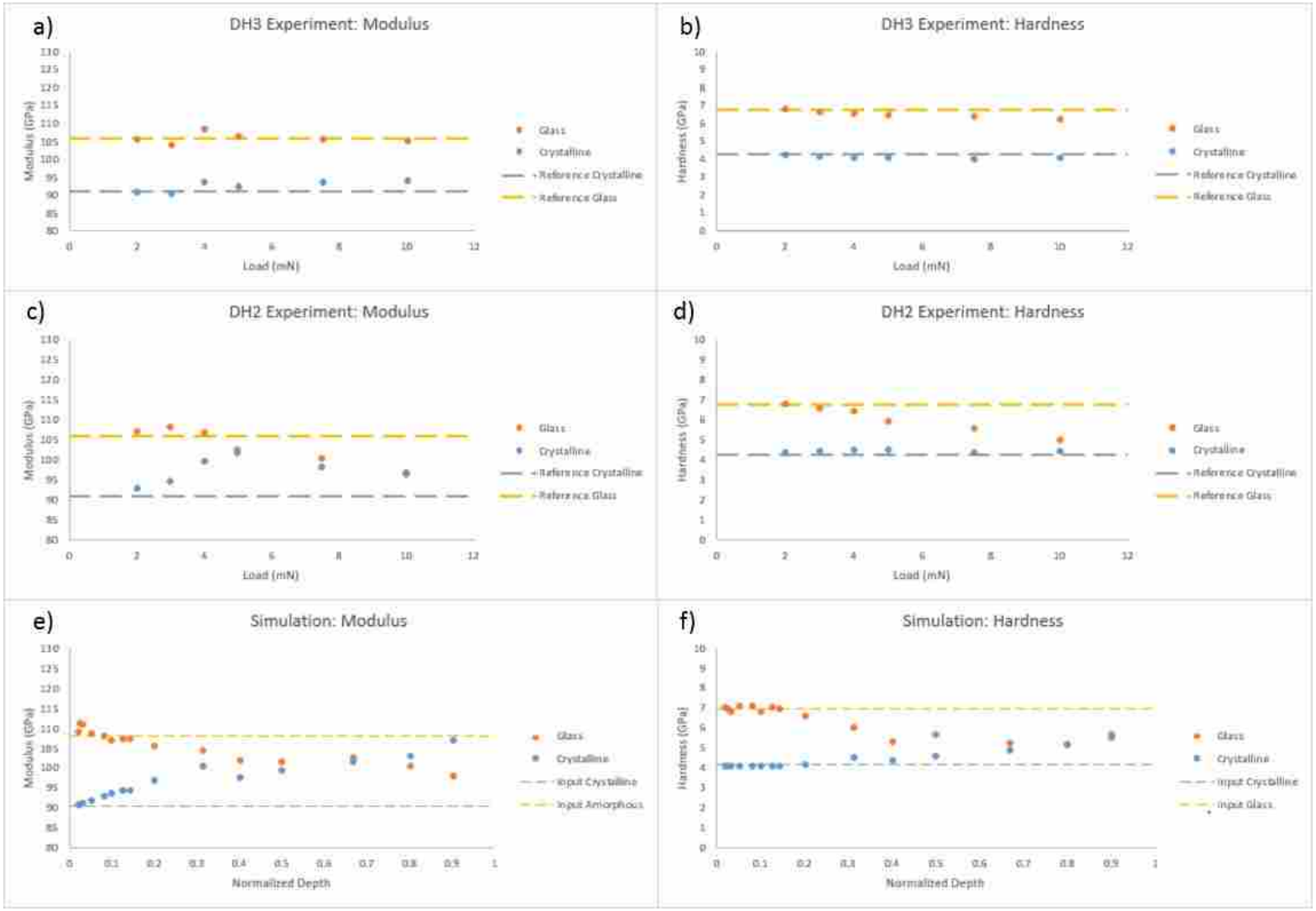

Figure 2-5: Hardness and modulus values
(a-d) Experimental and (e and f) simulated. Dashed lines signify the DH3 measured values at the lowest load for a)-d) and the inputted material properties for e) and f)

2.4 Discussion

2.4.1 Convergence to the properties of the composite

Originally, a cross-over of measured material properties was expected as it was thought that the indenter would begin to reflect the underlying phase. However, upon further investigation, once a sufficiently high load results in stress fields passing through the indented and underlying phase, the stress field begins to sample a complex microstructure of both phases resulting in a measurement of composite properties as a whole instead of individual phases. This was verified by Jonathan Gentile at SBU by using a large indenter on the DH1 phase at 10mN. Each phase was targeted and resulting hardness and modulus values were calculated. Because the dendrites are so small and the indenter so large, there is little to no significant sampling of individual phases even at the lowest loads. Figure 2-6 provide by Jonathan Gentile at SBU shows that regardless of which phase was targeted for indentation, measured modulus values are inseparable from each other and hardness values are close to converged as well. These values are also seen to have converged to almost the same values seen in the DH2 modulus values from Figure 2-5. Values are slightly higher in DH1 as a higher volume fraction of metallic glass exists which would suppose that the values will not trend as close to crystalline.

The measured values tend to converge towards the crystalline phase. If dendrite sizes are to be taken as the average radius of crystalline dendrites and dendrite spacings are taken as the average distance spanning domains between crystalline dendrites (from border to border and not dendrite center to center as most literature reports), then it was found that dendrite sizes are twice as large as dendrite spacings in the DH2 and DH3 specimens used in this work. With this

understanding, indentations will naturally sample more of the crystalline phase and measured values will reflect as such.

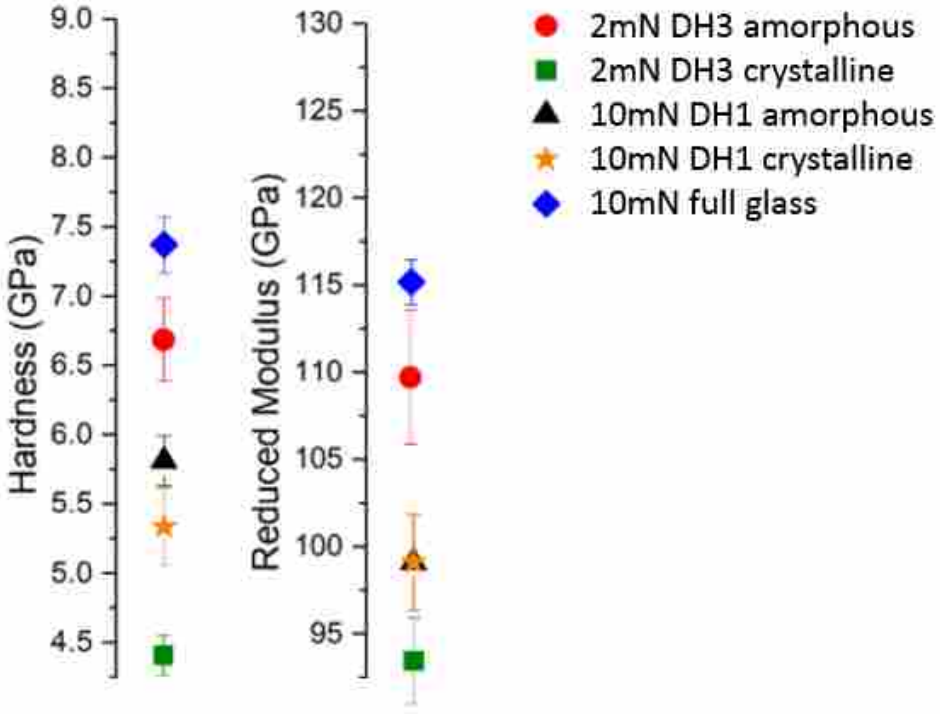

Figure 2-6: Comparison of measured hardness and moduli.
Indentation of DH1 composites demonstrates converging hardness values and converged modulus values on the composite properties as a whole. Figure was created by Jonathan Gentile at SBU.

2.4.2 Normalization of measured values

Experimental and numerical results are normalized so that they can be quantitatively compared on the same plot. For simulations, indented depth is already normalized by h/t. Hardness and modulus values are normalized against the expected hardness and modulus values from the material inputs (the yellow and grey lines from Figure 2-5e) and f) and explained above). For experimental data, the maximum indentation depth for each indentation is taken to be h_e; t_e is taken to be the average dendrite size when indenting the crystalline phase and the

average dendrite spacing when indenting the amorphous phase. Normalized depth is then calculated as h_e/t_e. These values were measured using SEM images of the indented samples. These values are listed in Table 2-3. Note again that the dendrite spacing here is measured as the average distance spanning the domains between dendrites as opposed to the dendrite center to center distance commonly reported in literature [53]. Hardness and modulus values were normalized by the average values measured from indentation of DH3 at its lowest load (yellow and grey lines from Figure 2-5a)-d) and explained previously)

Table 2-3: Average dendrite sizes and spacings.
From SEM images of indented samples.

	DH2	**DH3**
Dendrite Sizes (nm)	1500	5200
Dendrite Spacing (nm)	750	2500

When experimental and simulated nanoindentation measurements are able to be superimposed onto the same axes as shown in Figure 2-7, it is easy to see good agreement in measurements. The figure is split into 4 plots: one each for the measured modulus values for the amorphous and crystalline phases respectively and one each for the measured hardness values for the amorphous and crystalline phases respectively. Square data points reflect simulated results and circular data points reflect experimental results. Not only do numerical simulations agree with the experimental data, but different dendrite size composites (DH2 and DH3) are able to span normalized indentation depths in agreement with each other as well. The clearest agreement in data comes from measurements of the elastic modulus when indenting the glassy phase. Shown is a clear interaction between the two phases beginning at 15%-20% normalized indentation depth. Once these length scales are reached, the elastic zone begins to sample the underlying dendrite.

2.5 Summary

A combined simulated-experimental nanoindentation approach was taken to investigate the material properties of the individual phases in DH3 and DH2 MGMCs. Experimental nanoindentation of DH3 specimens at its lowest loads were verified by numerical modeling to accurately reflect material properties of the individual phases. As indentations are indented deeper into the sample, it was found that the elastic modulus begins to deviate from first before the hardness values begin to deviate. It was also found that when nanoindentation is loaded at higher loads and measured values begin to deviate, measured values will begin to converge to the properties of the composite as a whole.

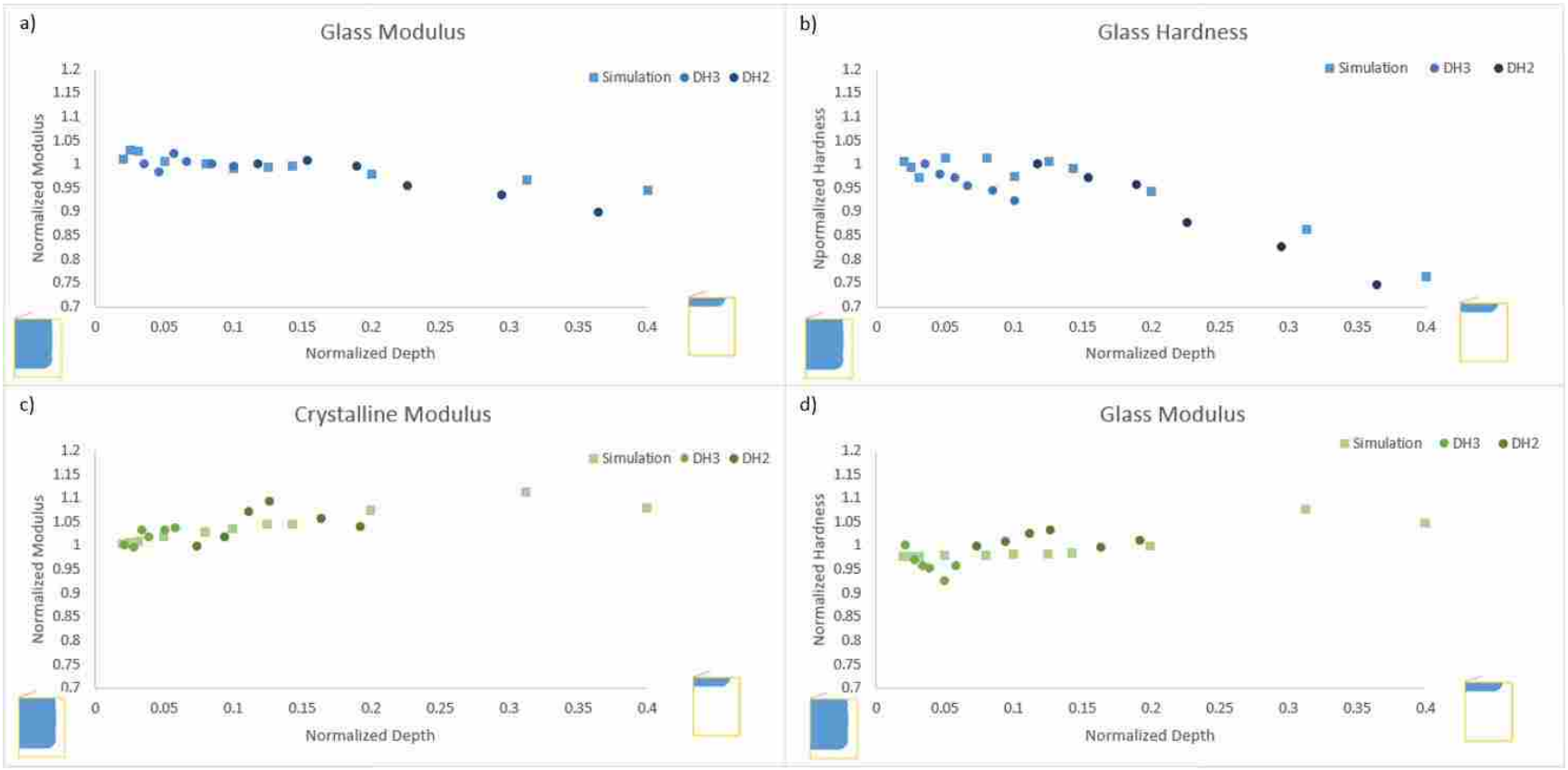

Figure 2-7: Comparison of simulated vs experimental values of hardness and modulus.
a)-b) are glass values and c)-d) show Crystalline values

3 EXAMINING THE MECHANICS RESPONSIBLE FOR STRAIN DELOCALIZATION IN METALLIC GLASS MATRIX COMPOSITES

3.1 Introduction

As explained in Chapter 1, the main goal of this work is to verify that the competition of rates seen in metallic glasses strained at high strain rates is also seen with the introduction of crystalline inclusions into the amorphous matrix. By doing so, we can simultaneously gleam correlations between microstructural variables and strain delocalization via competition of rates.

The STZ dynamics simulation method proposed by Homer et al. [22] is used to systematically vary dendritic structures. Tensile test simulations are run with changing dendrite lengths scales to investigate their effects on macroscopic and shear banding characteristics.

3.2 Method

3.2.1 Mimicry of dendritic structures in MGMCs

A variety of MGMCs have been developed with unique alloy composition and dendrite morphology via a variety of processing techniques [40], [41], [61], [99]–[102], [43], [45], [48], [49], [53]–[55], [58]. SEM images of DH3 composites [53] are used here to create the microstructure for the simulations in this work. SEM images are binarized, correcting any image defects during the process, and a variety of dendrite length scales and their effects on the shear banding process is examined. The length scales examined here are on the order of nanometer sized dendrites (see below). Although these dendrite sizes are smaller than those generally

studied, computational constraints limit the sizes that can be reasonably examined. That said, there are some examples that approach length-scales studied here [99] and the results in this work corroborate experiments at larger scales.

Systematic variation of dendritic structure is accommodated by providing a target or desired dendrite size for each simulation, scanning and scaling a random area in an image to achieve the target dendrite size, and then mapping the binary matrix onto the finite element mesh. Dendrite size (L) is approximated as the diameter calculated from the dendrite area. Although some discrepancy does exist between the binary matrix and triangular mesh, by using a fairly dense mesh (about 103000 elements), the effects are minimized (see Figure 3-1).

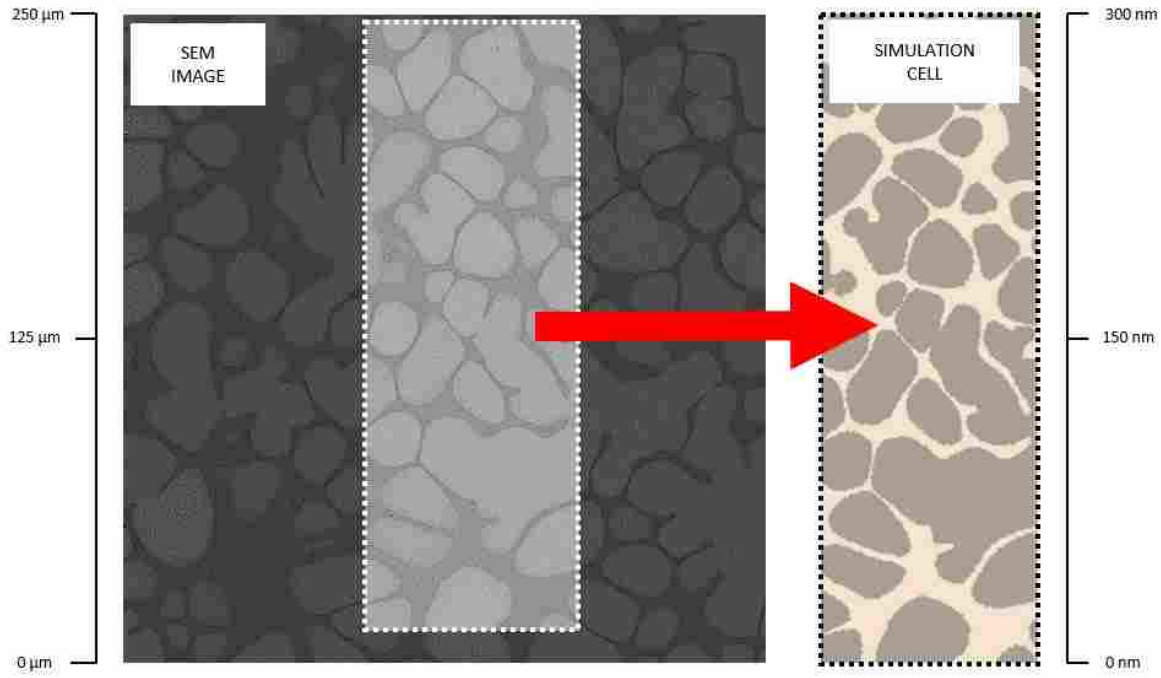

Figure 3-1: Using SEM images to systematically mimic and vary dendritic microstructure

3.2.2 Procedure

Simulations are run with varying dendritic size. 4 different levels of dendrite size are run and for each level, 3 different simulation cell morphologies are created that meet those values. Due to the stochastic nature of the modelling framework, identical models run multiple times could yield slightly various responses. As such, each morphology is run twice resulting in a total of 24 simulations. The microstructural variables and simulations are described in Table 3-1. Dendrite spacings and volume fractions are also reported in this table for reference, however, the rest of the paper will only refer to dendrite size as dendrite spacing scales with size and volume fraction is held constant. Example morphology from each level is shown in Figure 3-2.

Table 3-1: Systematic variation of dendrite microstructural features.

Simulation	Dendrite Size (nm)	Dendrite Spacing (nm)	Volume Fraction
1	7	17	64.6%
2	10	23	64.8%
3	16	38	64.8%
4	20	50	64.3%

3.2.3 Model inputs

2D simulations are strained under tensile loading conditions at a constant strain rate of 10^{-3} s^{-1} (or 0.3nm/s) along the long axis. The simulations are 300nm tall and 100nm wide. Because the modelling framework has not incorporated a failure mechanism, each simulation is simply strained to 0.035. At 0.035 strain, the specimen has been strained enough to characterize shear banding in the specimen.

Figure 3-2: Example morphology at each dendrite size labeled below each image

The STZ Dynamics model uses a kMC algorithm that requires a maximum time step. For this work, a maximum time step of 1s was used. This maximum time step is used to suppress any STZ activations that would require a time step larger than 1s. When this happens, the system steps forward by 1s, or a strain of 0.001. For a simulation 300 nm in height, this leads to a maximum possible displacement of 0.3nm per step [74].

Results from chapter 2 is used to calculate the required yield strengths and strain hardening rates as inputs for the crystalline phase in this model. Because a few combinations of yield strengths and strain hardening rates would match results from nanoindentation experiments and simulations, they were systematically varied between 0.9 GPa to 1.9 GPa and 0.05 to 0.3 respectively. Using Clausner's expanding cavity model [96], a map of resulting hardness values were calculated (see Figure 3-3). A few combinations of material properties could have been

chosen that matched experimental results closely. A yield strength of 900 MPa and strain hardening exponent of 0.3 was chosen to match reported strain hardening rates for high entropy alloys [103].

n \ Y	0.9	1.1	1.3	1.5	1.7	1.9
0.05	-31.58%					
0.1	-22.99%	-10.25%	0.58%	9.81%	17.81%	29.14%
0.2	-12.29%	-1.50%	9.93%	21.89%	33.58%	43.73%
0.3	-0.46%	12.84%	25.61%	37.04%	47.61%	57.58%

Figure 3-3: Systematic variation of yield strength and strain hardening exponent
The result percent error for calculated hardness using Clausner's expanding cavity model is shown [96].

Table 3-2: Model parameters for amorphous and crystalline phases

Property	**Symbol & value**
Amorphous parameters	
Shear modulus	μ = 35.69 GPa
Poisson's ratio	ν = 0.352
Debye temperature	327 K
Activation energy barrier	ΔF = 1.59 eV
STZ shear strain	γ_0 = 0.1
STZ volume	Ω_0 = 2.2 nm^3
Crystalline parameters	
Shear modulus	μ = 39.96 GPa
Poisson's ratio	ν = 0.33
Yield stress	σ_y = 900 MPa
Microstructure length	D = 50 nm
Burger's Vector	b = 2.858 Å
Empirical constant	a = 0.1
Hardening coefficient	n = 0.3

The parameters of the amorphous phase are calculated using the simulated strain rate and a slightly adjusted model provided by Harris et al. [39]. This provides an approximate yield strength of 2.1 GPa using an STZ volume of 2.2 nm^3 and an activation energy barrier of 1.59 eV. The shear modulus of the glass is 35.69 GPa, the Poisson's ratio is 0.352, and the Debye temperature is 327 K [22].

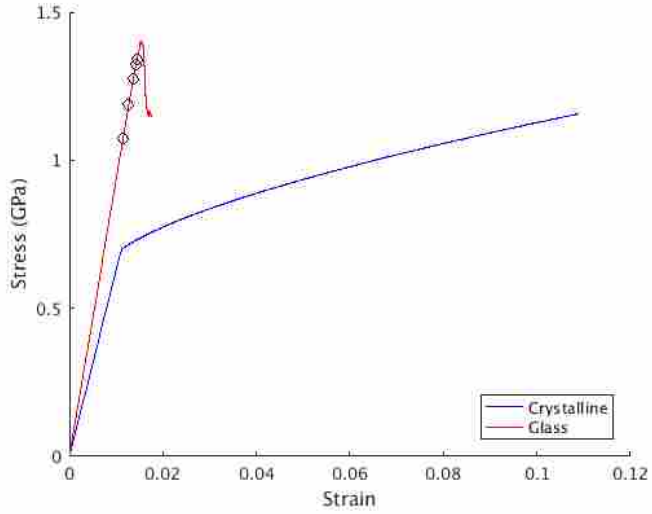

Figure 3-4: Characteristic stress-strain curves for the amorphous and crystalline phases Simulations created using material inputs for this chapter. Circles denote the first few STZ activations.

The parameters for the amorphous and crystalline phases are described in Table 3-2. For a more complete explanation of the material properties and how they influence the modelling framework, the interested reader is referred to [75], [104]. A characteristic stress-strain curve for the crystalline and amorphous phase is provided in Figure 3-4.

3.3 Analysis approach

After each simulation, macroscopic and shear banding characteristics are calculated and analyzed. This section describes the various characteristics

3.3.1 Macroscopic characterization

In this study, two measures have been classified as macroscopic in nature: localization index ('Γ') and two-point statistic localization (L_2). These measures help provide a general view of the specimen as a whole without measuring specific characteristics at the microscale.

3.3.1.1 Localization Index (Γ)

The localization index ('Γ') provides a general measure to help classify the distribution of plasticity throughout the specimen and is introduced in [105]. It is calculated using the following:

$$\Gamma = 1 - \frac{(\sum_n \gamma_n^2)^2}{N \sum_n \gamma_n^4} \tag{3-1}$$

γ_n is the plastic strain associated with each of the *N* elements of the sample. Γ ranges from 0 to 1 where 0 represents a totally uniform strain distribution and 1 represents strain being concentrated in an infinitely small region. 0.5 would represent a specimen that deforms with very homogeneous flow. Due to the nature of this measurement, any specimen that experiences any degree of localization will have similar values to that which may experience significantly more localization. That being said, there is some insight to be gained by any discrepancies in the values. This measure is calculated at the end of each simulation.

3.3.1.2 Two-point statistic localization (L_2)

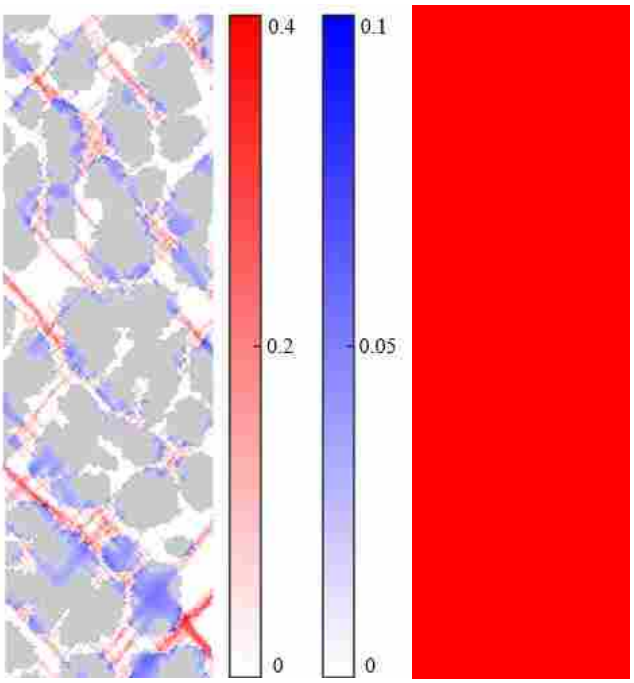

Figure 3-5: Autocorrelation example
a) Example of plastic scalar field distributed through a specimen. b) Autocorrelated field. The degree of localization can be calculated and given a scalar value by averaging the strain inside the square and dividing by the strain averaged outside the square.

The second measure to macroscopically characterize the specimens uses two-point statistics to characterize the degree of localization found during deformation. This is done by first calculating the Von Mises plastic strain component in each element and mapping to a 2D evenly spaced grid. This produces a scalar field $P(\vec{x})$, an example of which is shown in Figure 3-5. The two-point statistics are then generated by autocorrelation by evaluating the following [75]:

$$\mathrm{T}(\vec{x}) = \left(\frac{1}{\sqrt{n}}\mathcal{F}^{-1}\left\{\overline{\mathcal{F}\{P\}}\cdot\mathcal{F}\{P\}\right\}\right)^{1/2} \tag{3-2}$$

where n is the number of raster squares in P and $\mathcal{F}\{\quad\}$ is a fast Fourier transform. The overline signifies complex conjugation and the dot represents element-wise multiplication. The two-point statistic localization can be reduced to a single number by averaging the strain in an area around the center of the field in T and dividing by the strain averaged everywhere else in T (see Figure 3-5). The area around the center is chosen to follow [75] or a square with sides 5.3nm in length. The interested reader is directed to [75], [106], [107] for further details.

3.3.2 Shear banding characterization

After the simulations are run, the shear banding characteristics are analyzed. The plastic strains corresponding to each element in the finite element mesh is calculated every 5 steps. In the elements belonging to the amorphous phase, plastic strains are only accumulated by STZ activation and therefore any amorphous elements that accumulate plastic strain are counted as part of the shear banding network in a simulation. However, for the crystalline phase, by the end of the simulation, every element has accumulated some degree of plastic strain. Therefore, a strain threshold is implemented. Crystalline elements that do not meet this threshold are not counted as part of the shear banding process. Although the exact value is subjective, we examined varying levels and ultimately picked 0.03 strain as the threshold. It is relatively straightforward to see how shear bands grow and choose the value that best demonstrates shear banding.

Elements that meet the strain threshold and are connected by at least one node are considered to belong to an individual shear band. After grouping elements into individual shear bands, the shear band areas are calculated and only those shear bands that meet a minimum shear band size are included in the shear band characterization analysis. The goal with this size

threshold is to reduce the likelihood of mistakenly counting one shear band nucleus as multiple smaller nuclei while at the same time still distinguishing the emergence of multiple distinct nuclei that eventually join together. The threshold also helps eliminate misleading propagation rates when shear band nuclei still consist of just a few STZs. For example, the addition of one STZ to another lone STZ would result in a 200% growth rate. As is the case with any nucleation type growth, size thresholds are somewhat subject to interpretation. Li et al [108] reports a critical nucleation size of 10-20 nm in diameter by simulating a mode I fracture using molecular dynamics. Harris et al. [39] reports critical nucleation sizes anywhere from 15-30 nm^3 using STZ dynamics when strained at 10^{-3} s^{-1}. A brief study by varying different nucleation sizes (15-29nm^2) and analyzing the resulting shear band nucleation rates yielded little variation. As such, a threshold of 15nm^2 is chosen (or a cluster of roughly 5-7 STZs).

Once shear bands are thresholded, each new shear band and all its elements are classified and assigned a shear band identity. As the simulation progresses, shear band identities are maintained unless multiple shear bands merge into a single shear band. When this occurs, the identity of the largest shear band is maintained and all elements belonging to the now singular shear band follow this identity. After elements have been assigned to shear bands and evolution tracking of shear bands have been stored, it is somewhat straightforward to then measure the following shear banding characteristics.

3.3.2.1 Number of shear bands (#SBs)

The number of shear bands can easily be counted and provides one measure of nucleation rate. The number of shear bands can be counted in two ways: 1) the number of shear bands that nucleate throughout the simulation and 2) the number of shear bands that exist at the end of the simulation. These numbers differ because many shear bands that nucleate will eventually merge

with another shear band. Therefore, the number of shear bands that nucleate throughout the simulation is expected to be significantly higher than the number of shear bands at the end. The number of shear bands is divided by time to provide a nucleation rate.

3.3.2.2 Propagation rates ($\dot{\varepsilon}_{SB}$)

There are numerous ways to calculate the overall growth rate of shear bands. In this work, the measure of propagation rate is represented by calculating the rate of change of the area averaged strain towards the end of the simulation for the largest shear band. This is done by calculating a linear fit of the area averaged strain vs. time and taking the slope of that line. Shear bands that grow from joining together with another shear band are ignored. Towards the end of the simulation, strain rates of dominant shear bands are relatively constant which provides a more consistent propagation rate value. In this work, of the total 3.5% strain, only the last 0.3% strain is used to calculate this measure as strain growth rates are relatively constant after this point. Only the rate of strain accumulation in the largest shear band is evaluated as this is identified as the run-away shear band. Using the largest shear band or a few of the largest shear bands yields little variation. This measure will provide insight as to how shear band growth is affected by microstructural sizes.

3.3.2.3 Involvement of the crystalline phase (C)

Unique to this paper, the crystalline phase's degree of involvement in the overall shear banding process is reported. This is reported as the overall percentage of shear band elements that are crystalline. This can help provide some further light on the competition of shear band nucleation and propagation rates.

3.3.2.4 Proportion of strain localized in 3 largest shear bands (L_1)

The fraction of strain that is accumulated by the 3 largest shear bands at the end of the simulation is measured. This will describe somewhat the degree of localization in a specimen and how shear banding participates in strain accumulation.

3.3.2.5 Shear band domination (D)

During the early stages of shear banding in MGMCs, numerous shear bands may compete before a run-away shear band occurs. During this competition, shear bands may alternate between which shear band is propagating the fastest for periods of time. The number of shear bands that take their turn dominating a simulation is calculated and reported here. This can provide insight as to how quickly strain is localized in a shear band.

3.4 Results

Figure 3-6 shows examples of simulations run at each microstructural size. The images of the dendritic structure are taken at the end of the simulation (or 0.35 strain). The dendrites are denoted by gray and closely resemble those seen in experimentation. The white areas denote amorphous regions of the composite. The blue and red fields are the plastic strains seen by the crystalline and amorphous phases respectively. These images allow side-by-side shear banding comparison and clearly demonstrate greater localization with the larger dendrites.

A couple observations can be made from this figure. First, it is quite easy to see that the degree to which the crystalline phase participates in shear banding is much higher in the smaller dendrite composites. The larger dendrite composites tend to only propagate through a dendrite when it traverses narrow or short sections of the dendrite. Shear bands that encounter the full

thickness of a large dendrite seem to often be obstructed and kept from initiating further shear banding into and through the dendrite.

A second observation can be seen by noting the variation in vibrancy of coloring. The larger dendrite simulations see brighter red and blue signifying higher levels of strain achieved by a smaller group of elements. This indicates a higher degree of strain localization found within these larger dendrite specimens.

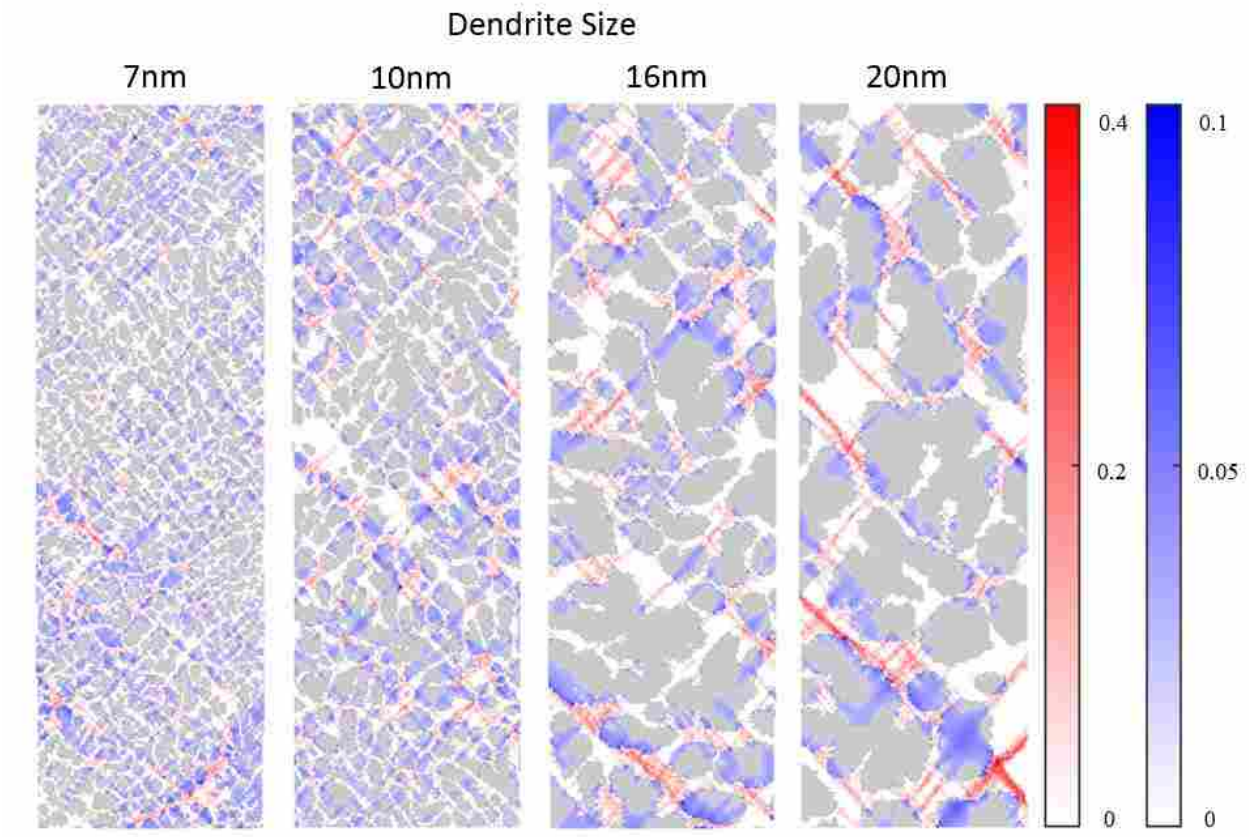

Figure 3-6: An example of each microstructural size evaluated
The blue and red fields delineate the plastic strain in the crystalline and amorphous phases respectively (shaded gray areas are crystalline and white areas are amorphous). Corresponding stress-strain curves are shown on the left.

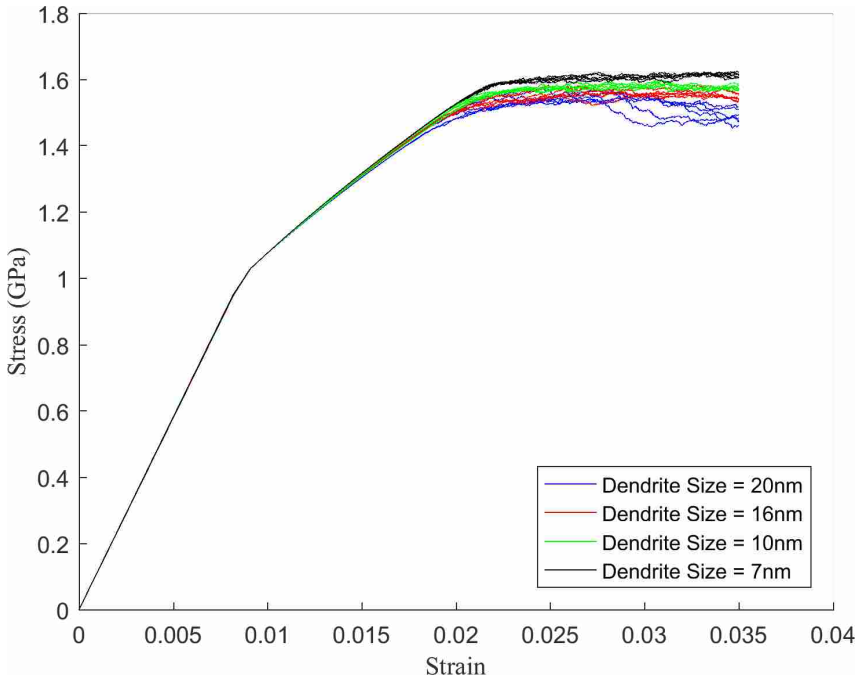

Figure 3-7: Stress-strain curves for all simulations

Stress strain curves for all simulations are shown in Figure 3-7. Yield stresses are seen to increase as dendrite sizes decreases. This is not consistent with what was expected. Due to a higher participation of the crystalline phase as dendrites get smaller as evident from Figure 3-6, it would be expected that yield points would decrease. However, due to lack of a failure mechanism in the model, the crystalline phase continues to strain harden and in fact the opposite is true here. By slowing down shear band propagation rates, shear band growth is delayed and higher stresses can be reached.

3.4.1 Macroscopic measures of strain localization

3.4.1.1 Localization Index

Localization indices were measured according to Equation (3-1) for each simulation. A box plot of the measured localization indices binned into different dendrite sizes is shown in

Figure 3-8. This box plot and subsequent box plots use a line through the box to denote the median value. The tops and bottoms of the boxes mark the upper and lower quartiles of the distribution with maximum and minimum values denoted by the extended whiskers. Any statistical outliers will be marked with a cross (+).

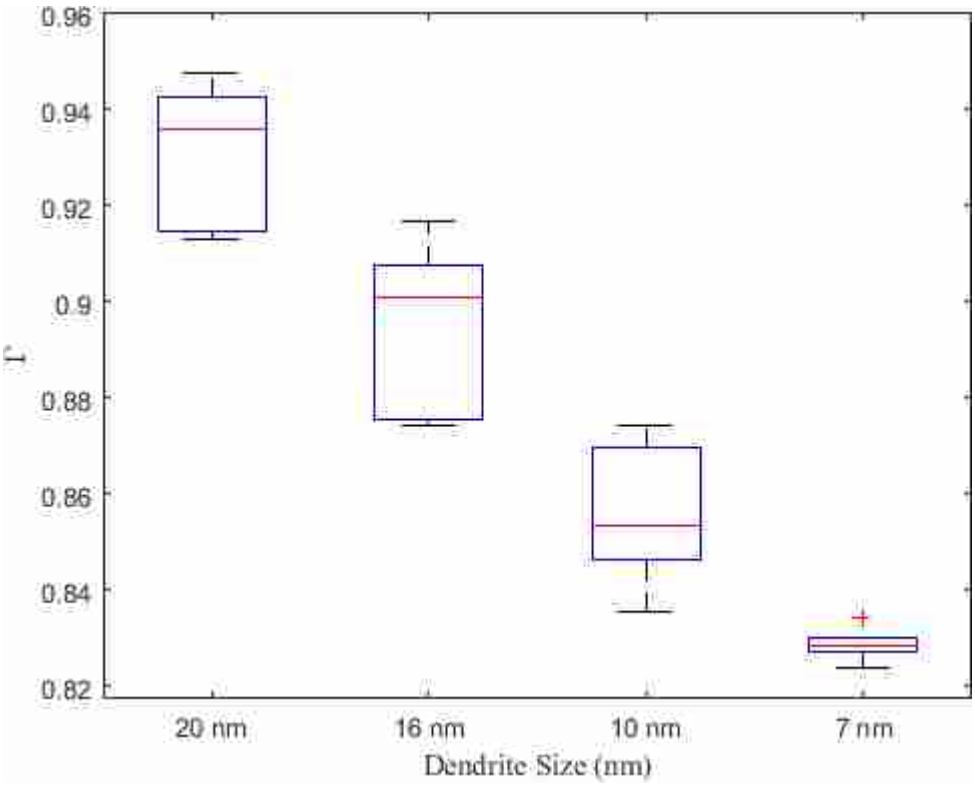

Figure 3-8: Box plot of the localization indices in each simulation arranged by dendrite size. This indicates increased strain localization is evident in simulations with larger dendrites.

Although the numbers are fairly close in value, there is a strong downward trend as the dendrites get smaller. In other words, the degree of localization decreases with dendrite size. Also, due to the nature of the measurement, results were really only expected to span $0.6 < L_2 < 1$ at the most so the measured distribution is actually quite telling. When dendrites are large, the median localization index is as high as 0.936 (again, for reference, a value of 1 would have strain concentrated in an infinitely small area). As the dendrites get smaller, the localization index also

gets smaller with median values reaching 0.830 when dendrite sizes are 7nm. There is still some localization in both cases although the magnitude has decreased. This is also verified in the following two-point statistical measure of localization.

3.4.1.2 Two-point statistic localization

Measured values for two-point statistic localization was also found to decrease with decreasing dendrite size. This numerically confirms what can be visually seen from strain maps (Figure 3-6). Numerical values are quite small as the ratio of inner to outer area used to calculate this ratio was also small and so values shown here are appropriate. For the large dendrites, a median value of 0.00444 is calculated. This decreases to 0.00343 for the small dendrites. The two-point statistical measures of localization for the simulations are shown as a box plot in Figure 3-9.

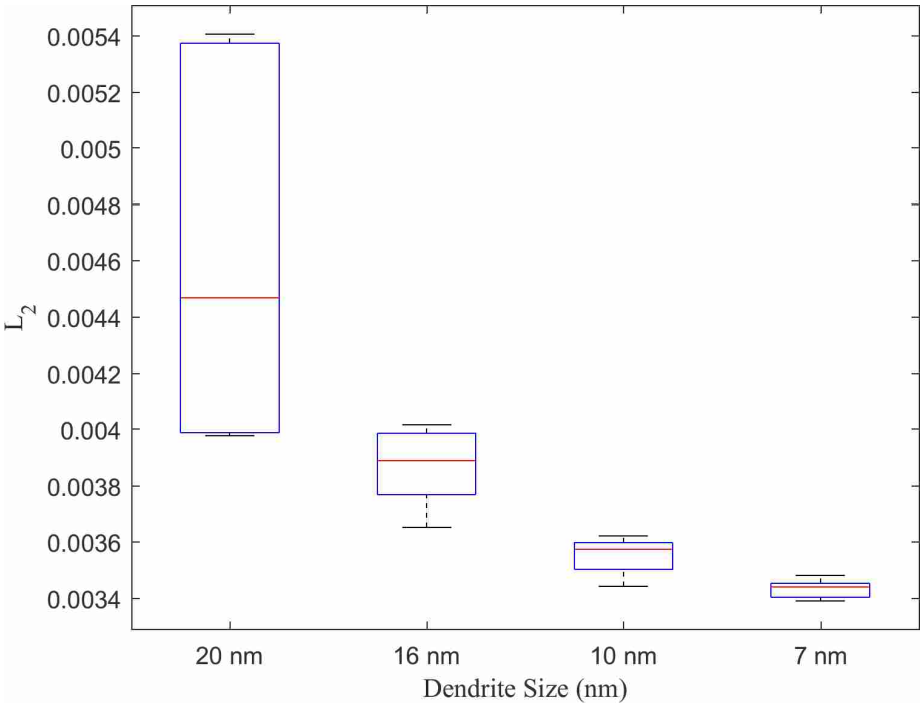

Figure 3-9: Box plot for a measure of localization using two-point statistics
Arranged by dendrite size. This verifies that larger dendrites experience higher degrees of strain localization.

3.4.2 Shear band characteristics

Shear band characteristics were calculated as described in Section 3.3.2. These measures were averaged and are shown in Table 3-3.

Table 3-3: Measured shear band characteristics

L (nm)	#SBs	$\dot{\varepsilon}_{SB}$ (s^{-1})	C (%)	L_1	D
20	1.8	0.35	26.5	0.82	56.5
16	2.6	0.0063	37.6	0.75	78.8
10	3.9	-0.014	42.3	0.62	110.7
7	4.4	-0.059	45.5	0.53	118.2

3.4.2.1 Nucleation rate (#SBs)

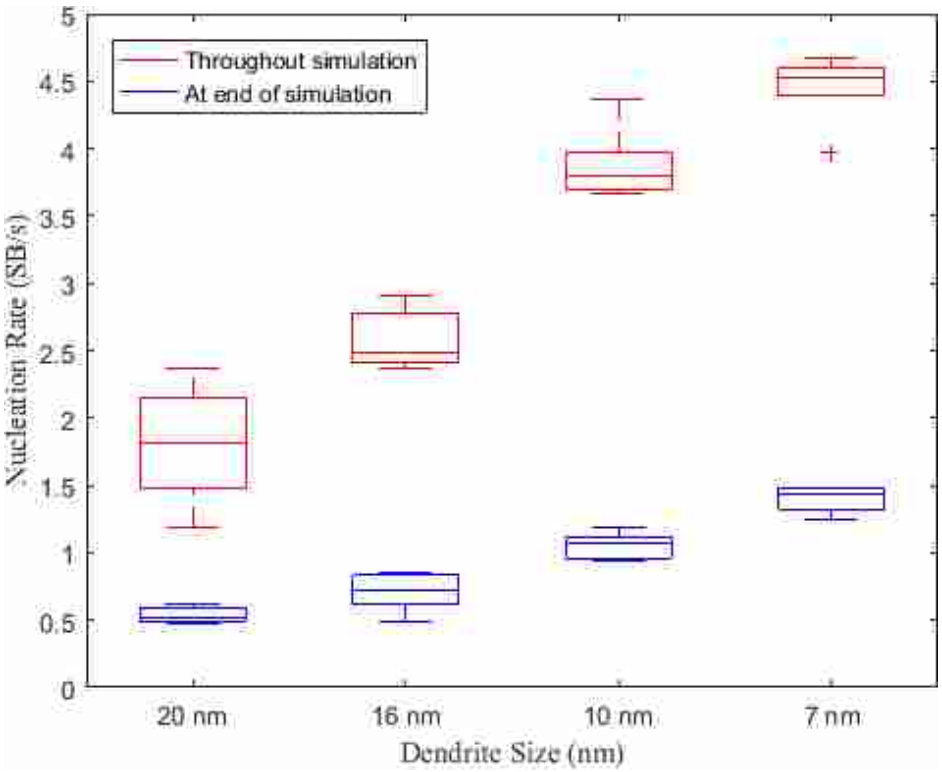

Figure 3-10: Box plot of measured nucleation rates arranged by dendrite size
Illustrated by counting the number of shear bands that nucleate throughout the simulation (in red) and exist at the end of the simulation (in blue).

After the simulations were completed, the number of shear bands were counted. They were then divided by the simulation time to provide a nucleation rate. These rates are illustrated using box plots shown in Figure 3-10. Red boxplots show the number of shear bands that nucleate throughout the simulation whereas blue boxplots only count the number shear bands found at the end of the simulation. These numbers are different because shear bands that nucleate early on can merge with other shear bands as the specimens are strained. Table 3-3 shows average nucleation rates calculated using the number of shear bands that nucleate throughout the simulation. Clearly, as dendrite size decreases, there are more shear bands. This matches expectations and forms a good measure of nucleation rate.

3.4.2.2 Propagation rate ($\dot{\varepsilon}_{SB}$)

The average rate of strain accumulation of the largest shear band is calculated for all the simulations. This measurement is used as a representation for shear band propagation rates and results are shown in Figure 3-11. The propagation rate measures how the area average strain of the shear band changes over time. Therefore, a negative rate can be calculated if additional strain elements that join the shear band have a strain lower than the average strain in the shear band in the step prior. This does not necessarily mean that the shear band is no longer growing but that the rate at which it is growing at has decreased. The larger the dendrites, the larger the propagation rate and the larger the spread of results. There is strong downward trend despite some overlap. When dendrites are large, the median rate of strain accumulation is 0.29 % s^{-1}. When dendrites are small, the median rate of strain accumulation is -0.04 % s^{-1}. The rate of decrease of propagation rate between different microstructural sizes decreases quickly when dendrite sizes are still large. It decreases at a slower rate when dendrite sizes are small. Also, at

smaller dendrite sizes, the largest shear band has little to no strain accumulation. These observations suggest a convergence of rates.

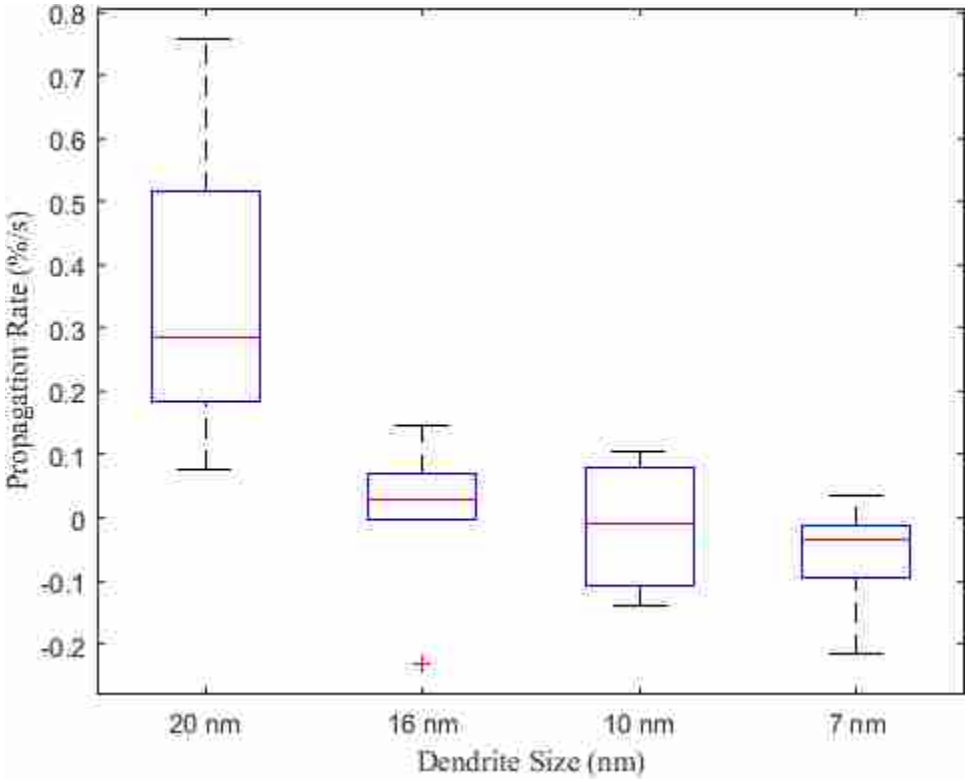

Figure 3-11: Box plot of propagation rates arranged by dendrite size

3.4.2.3 Involvement of the crystalline phase (C)

The involvement of the crystalline phase is measured as the percentage of strain in the shear band elements that accumulated by the crystalline phase. The measurements are illustrated in Figure 3-12. As dendrites get smaller, the crystalline phase participates more in the localization. At the highest, dendrites account for more than 45% of plastic straining in shear bands. When dendrite sizes are 20nm, the median crystalline involvement is 26.5%. At 16nm, the next size down, the crystalline percentage increases drastically to 37%.

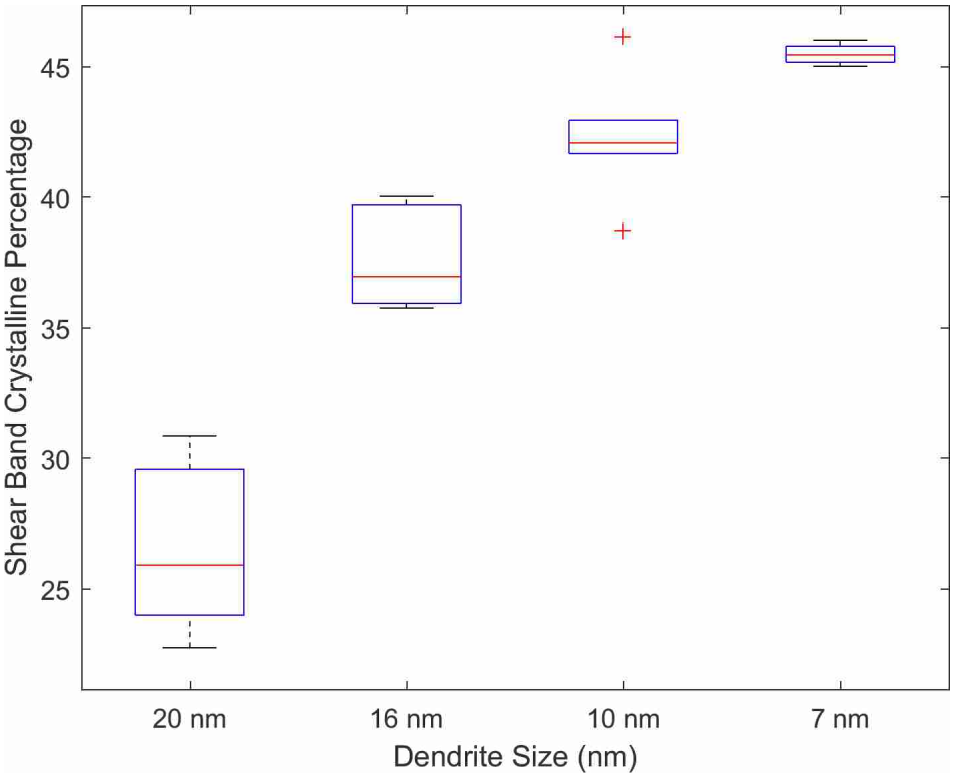

Figure 3-12: Box plot of crystalline phase involvement in shear banding
Arranged by dendrite size.

3.4.2.4 Proportion of strain in the 3 largest shear bands (L_1)

The fraction of total strain in the 3 largest shear bands is measured at the end of the simulation. Measurements are portrayed in Figure 3-13. Even as total strain in all shear bands increases, the fraction of strain taken by the 3 largest shear bands also increases suggesting greater localization than this data portrays. At the highest, a median of 81.5% of total strain is carried by the largest shear band. This number drops to 56% at the smallest dendrite sizes. The inset in Figure 3-13 shows measurements of the fraction of strain taken by the largest shear band only. Although there is a downward trend, it is not as convincing. It is thought that this is attributed to the fact that some simulations see one shear band accumulating most of the strain whereas others still see significant growth in multiple shear bands even at the end of the simulation. This provides a smattering of results regardless of dendrite size.

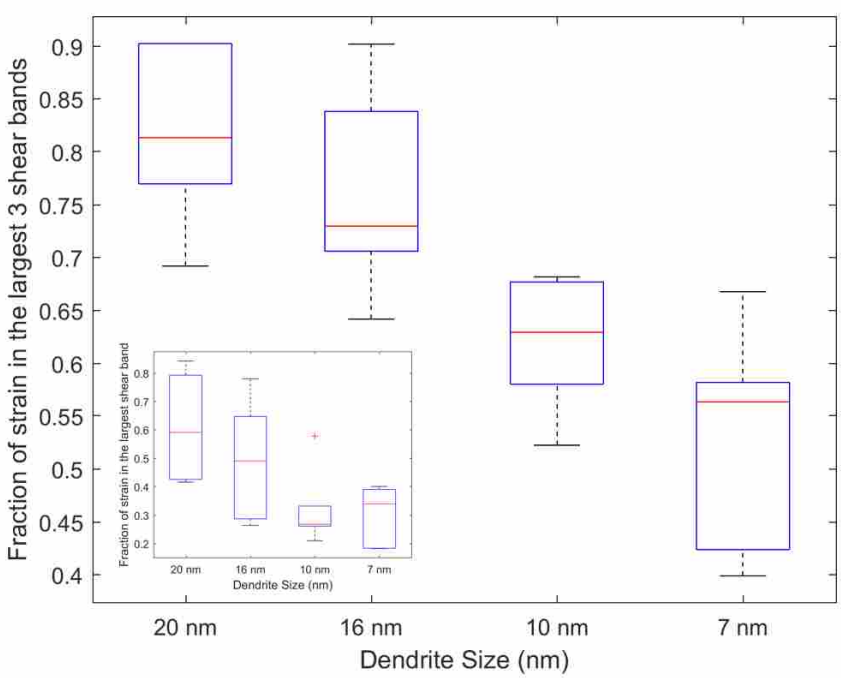

Figure 3-13: Box plot of fraction of plastic strain by 3 largest shear bands
Arranged by dendrite size. Inset shows fraction of strain taken by largest shear band.

3.4.2.5 Domination of shear bands (D)

During the early stages of deformation, different shear bands will dominate the plastic deformation of the specimen. The number of shear bands that dominate during the entire simulation is counted. Each time the growth rate of a shear band becomes the highest over a 5 step window, it is counted as a dominant shear band. Shear bands are only counted once. Results are shown in Figure 3-14. As dendrite sizes decrease, the number of shear bands that have at one point been dominant has increased. This suggests greater competition between shear bands.

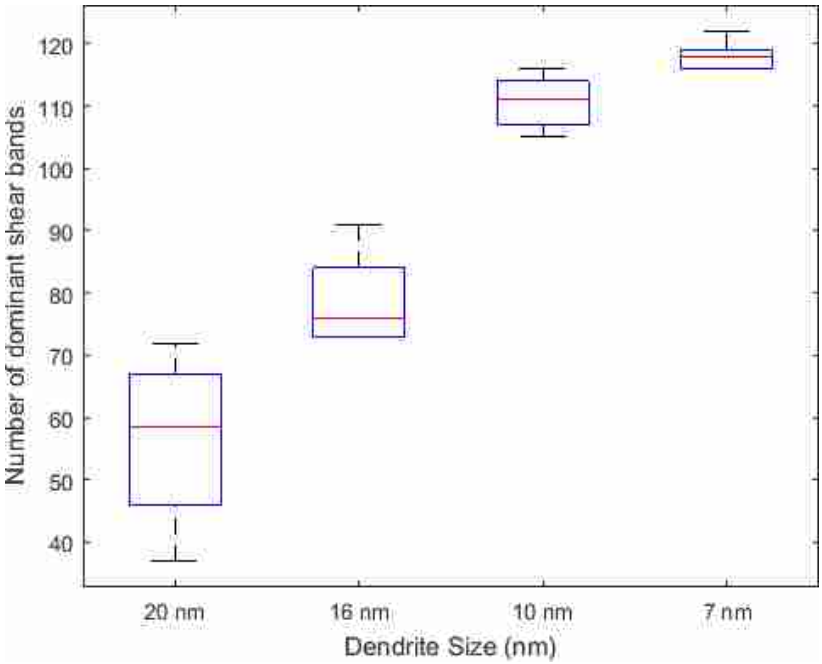

Figure 3-14: The number of shear bands that dominant plastic deformation

3.5 Discussion

3.5.1 Competition of rates

As mentioned previously, the competition of shear band nucleation and propagation rates are of interest in this work. This competition of rates has previously been demonstrated in purely amorphous metals strained at high rates [35], [39]. This work demonstrates that the same phenomena exists in MGMCs and sheds light on the underlying mechanisms behind strain delocalization. Additionally, this contrasts other views based solely on matching length scales [53]. These simulations enable a detailed view of the characteristics of shear banding in MGMCs. Further, the stochastic nature of the simulations allows some variability in results, which allows an examination of the effect of an averaged microstructural quantity rather than unique and specific conditions.

Nucleation and propagation rates are superimposed onto the same figure using normalization by their respective largest calculated values, shown in Figure 3-15. This figure demonstrates the competition of rates previously seen in metallic glasses at high strain rates. The relationship between dendrite size and these shear band characteristics demonstrate strong support for the hypothesis that an introduction of the crystalline phase results in strain relief via two mechanisms: 1) By lowering the propagation rates of shear bands and 2) by increasing the nucleation rates of new shear bands. The net effect is that the dendritic phase works to limit shear band propagation rates and encourage shear band nucleation rates resulting in reduced accumulation of strain in 1 or a few shear bands as seen in purely amorphous specimens.

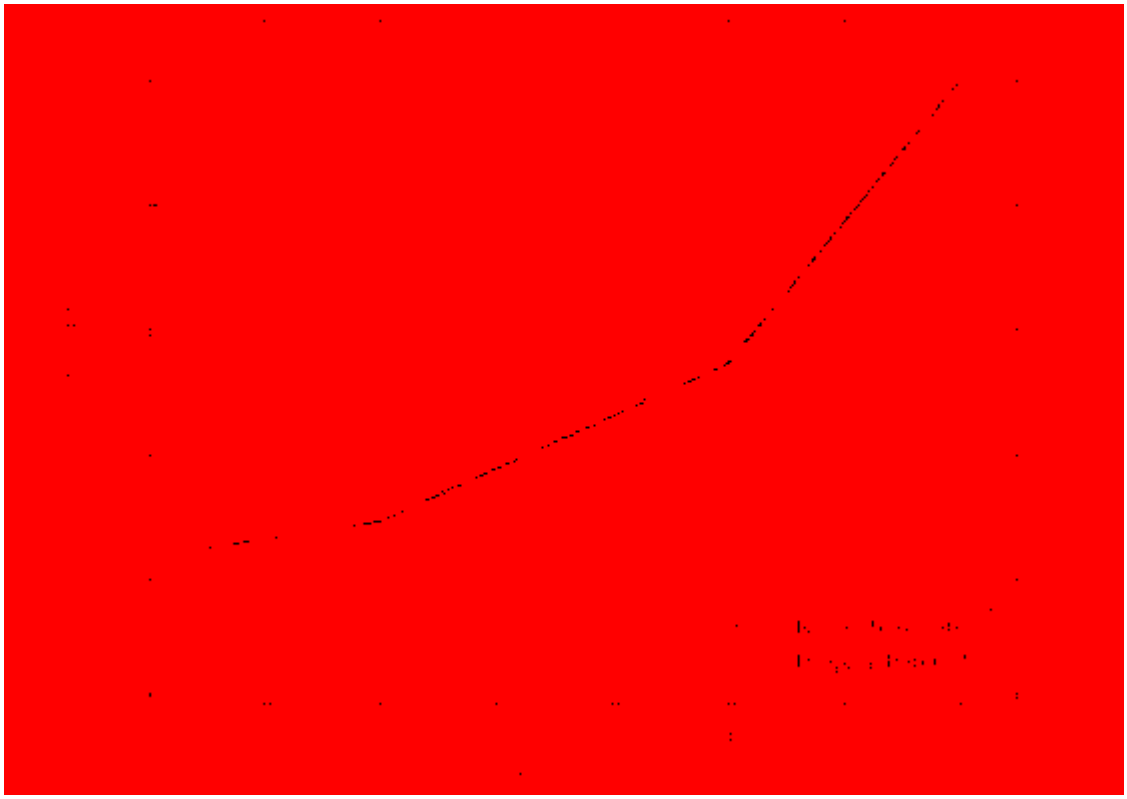

Figure 3-15: Competition of rates
Comparison of mean values of measured nucleation (blue) and propagation rates (orange). The relationship of dendrite sizes with nucleation and propagation rates supports the hypothesis that increased homogeneous flow is a direct result of strain relief by competition of rates.

For the dendrite sizes examined here, there is clearly a lack of local minima or maxima for shear band nucleation or propagation rates. In other words, there is no optimal microstructural size that works best to delocalize strain. This contrasts with reported optimal matching of dendrite length scales and shear band crack initiation sizes [53]. For the data shown, there is greater homogenization of strain the smaller the dendrites. These trends suggest that attempts at decreasing dendrite size experimentally may result in increased shear banding and strain delocalization.

This work suggests that the mechanism responsible for strain delocalization in MGMCs is the competition of nucleation versus propagation rates that work to limit strain accumulation in one to a few shear bands. As a direct result, this work then also proposes the method for greater strain delocalization in MGMCs is two-fold: 1) encourage shear band nucleation throughout the specimen and 2) decrease the rate of growth of shear bands. The question then remains, what exactly does encourage shear band nucleation to occur? And of course consequently what then discourages them to accumulate more strain once nucleated?

3.5.2 Examination of shear banding in MGMCs

One of the great benefits of using numerical simulations is the ability to examine much smaller time and length scales. This allows us to resolve mechanics not visible to experimentation such as the early stages of shear banding. Of particular interest here are understanding specific conditions that encourage shear band nucleation and propagation.

To better understand the mechanisms behind the competition of rates, we examine the conditions for initiation of STZs, nucleation of shear bands, and growth of shear bands.

3.5.2.1 Initial STZ activations

Snapshots of stress fields immediately before and after the first STZ activation in two example simulations at two microstructural sizes are shown in Figure 3-16 and Figure 3-17 (large and small dendrites respectively). Light yellow fields denote areas of higher stress. The red dots signify the first STZ activation in b) of these figures. Due to the nature of the STZ dynamics modelling framework, areas of high stress are, although not guaranteed, much more likely to experience an STZ activation than others. This is verified by the first STZ activation happening in one of highest stress concentrations on the map. This is consistent with what has already been noted in literature [109].

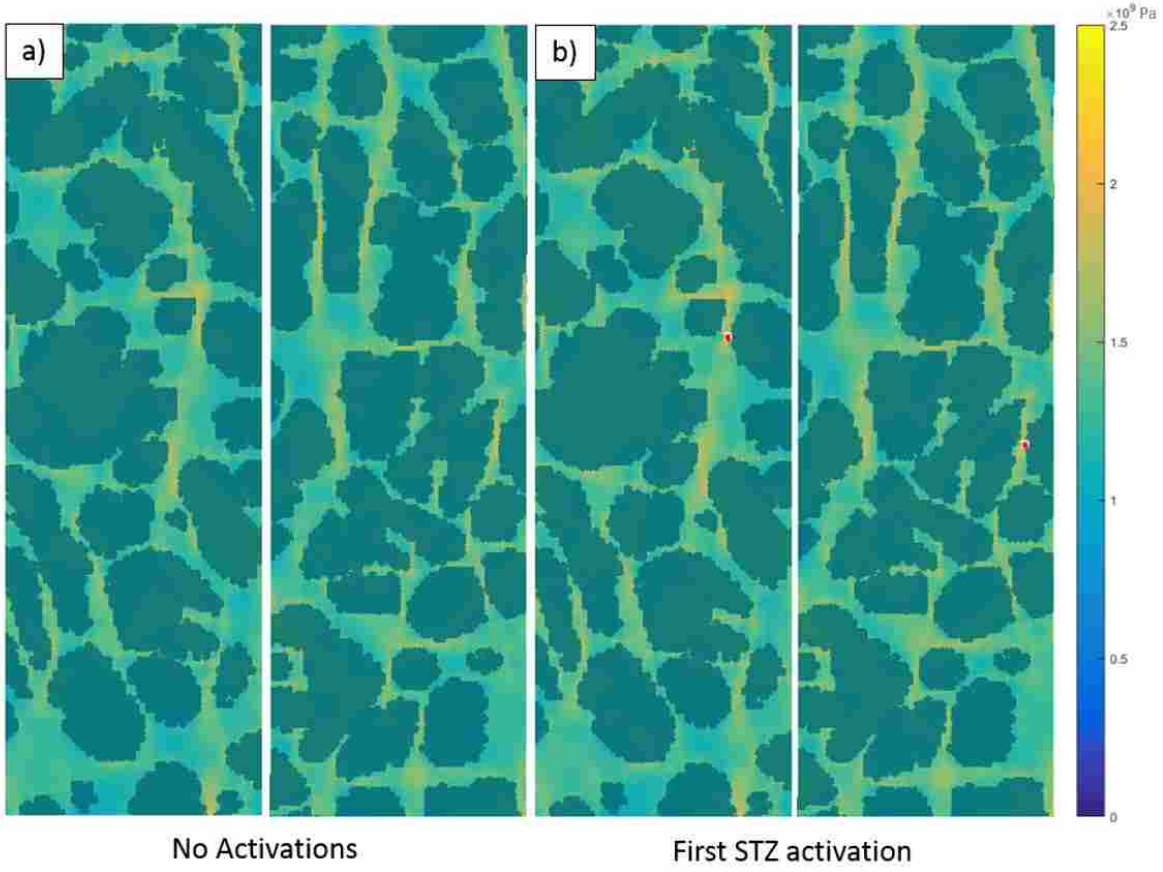

Figure 3-16: Examining the stress-fields in 2 example simulations with large dendrites a) immediately prior and b) after the first STZ activation. Red arrows point to areas of high stress concentrations and red dots show where the first STZ activation occurred.

When examining Figure 3-16, stress concentrations are particularly prevalent where there exist dendrites spanning both sides of a glassy domain along a 45° angle to the longitudinal axis or planes of highest resolved shear stress. Stress concentrations are higher the smaller the domain. Therefore, it can reasonably be inferred that in order to disperse STZ activations throughout the specimen, smaller domains will provide a larger number of desirable sites for STZ activations for uniaxial tensile loaded specimens. This could be achieved successfully with many round small dendrites.

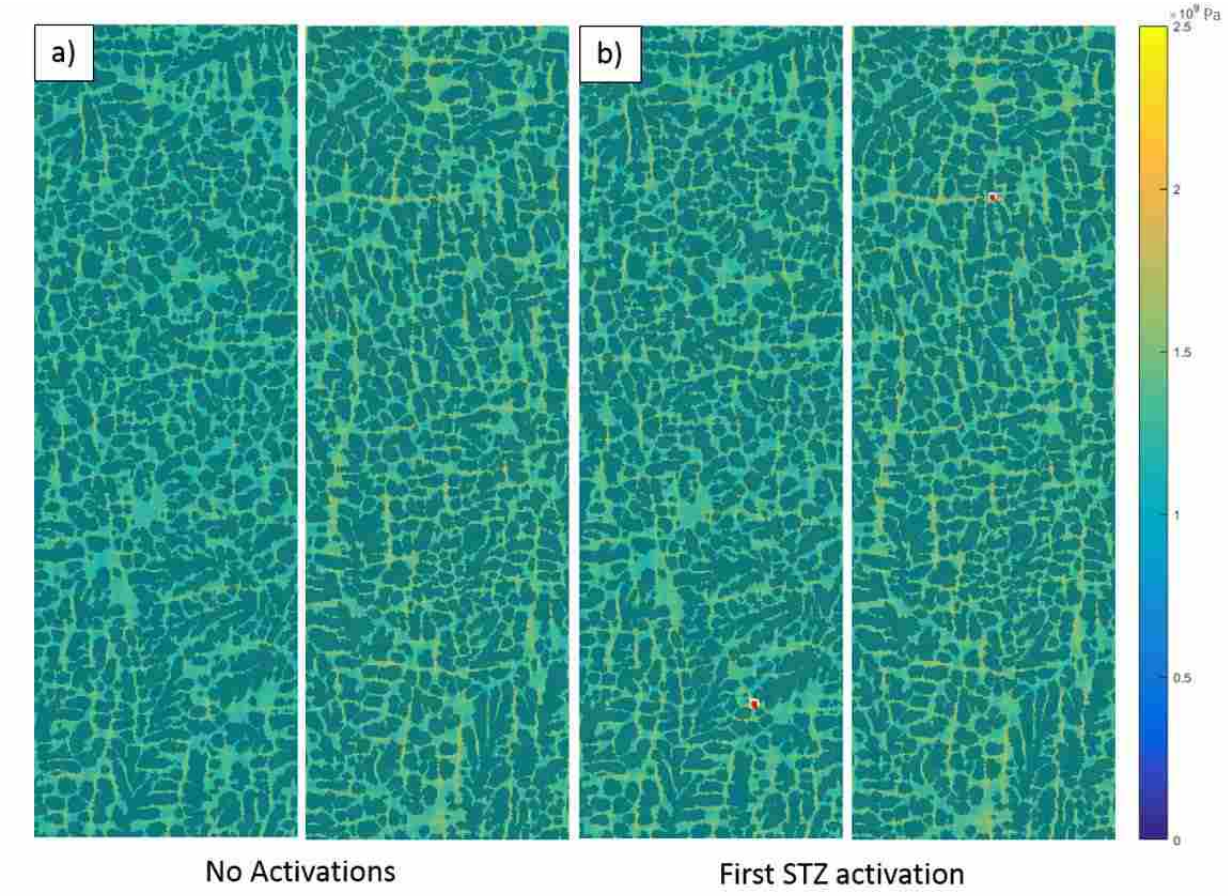

Figure 3-17: Examining the stress-fields in 2 example simulations with small dendrites a) immediately prior and b) after the first STZ activation. Red arrows point to areas of high stress concentrations and red dots show where the first STZ activation occurred.

Conversely, when looking at Figure 3-17, there is an increased number of high stress sites although the magnitudes are lower. This is verified in Figure 3-18. Figure 3-18 shows a plot of the maximum local Von Mises stress values in the specimen over time. This demonstrates that stress values are on average lower when dendrites are small. The inset in this figure also shows that stress concentration levels are higher before the first STZ activation in simulations with large dendrites than simulations with small dendrites (see inset in Figure 3-18). This means that STZ activations have less reason to cluster and therefore operate collectively in a more homogeneous manner in specimens with smaller dendrites as stress concentrations are lower in magnitude.

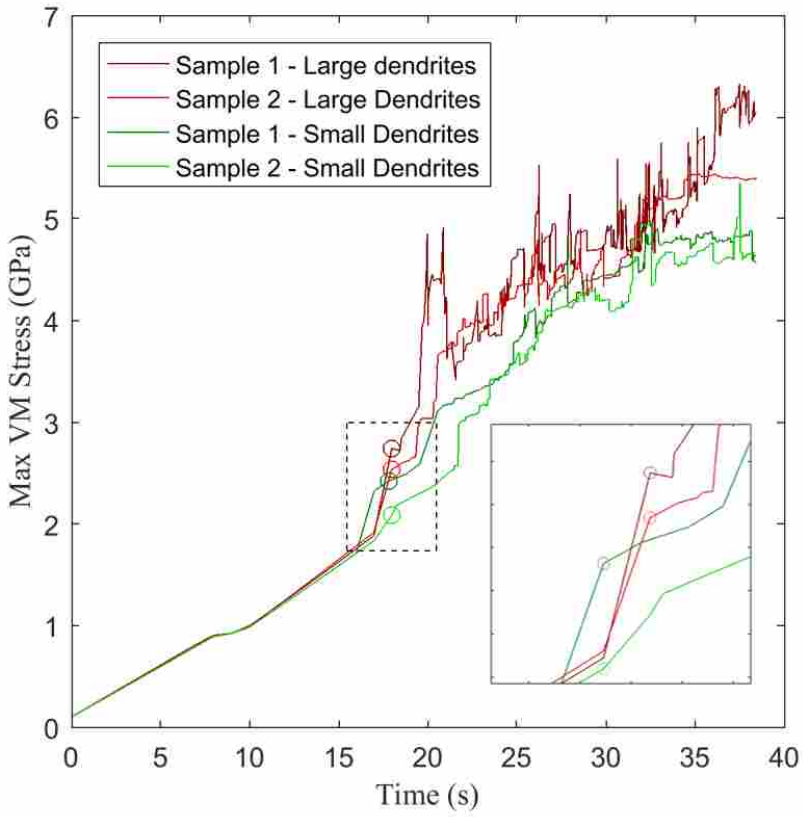

Figure 3-18: Comparison of maximum Von Mises stresses
Comparisons between two example large and two example small dendrite simulations are shown. Inset denoted by black dashed box shows stress concentrations as a result of the first STZ activation in each simulation. Circles denote first STZ activations in each of these simulations.

3.5.2.2 Shear band nucleation or STZ clustering

STZ clustering in MGMCs occurs in a different fashion than in pure amorphous metals. In monolithic metallic glass, STZ clustering happens much faster and with far fewer clusters [110]. In MGMCs, due to restricted domains and an increased number of stress concentrations from elastic mismatches, STZ clustering is encouraged to occur for an extended period of time. This is demonstrated in Figure 3-19. This figure shows the number of shear bands that exist as the simulation progresses. The shear band nucleation stage exists for as long as the number of shear bands are growing. When the number of shear bands begin to decrease, shear bands are now propagating and absorbing other shear bands and the STZ clustering stage has ended. Where shear band growth is the governing stage in amorphous metals, STZ nucleation is the governing stage in MGMCs.

For the simulations run here, the shear band nucleation stage is longer for MGMCs with smaller dendrites (see Figure 3-19). When dendrite sizes are decreased, the number of suitable nucleation sites increases. This encourages shear bands to nucleate in more areas. The number of shear bands in the simulations with larger dendrites increase more quickly in the beginning. However, they also peak earlier in the simulation as shear bands begin to run away and absorb other shear bands at lower stress levels.

As STZ clustering is examined, there seems to be no reason for one region to be more likely to accumulate STZ clusters than any other region in the specimen. After the first few initial STZ activations throughout the specimen, the choice of which STZ will first accumulate more STZs seems to be at random suggesting homogeneous deformation during this early stage.

And no significant trends were found as to the choice of which shear band nucleus will continue to grow in size and which will not.

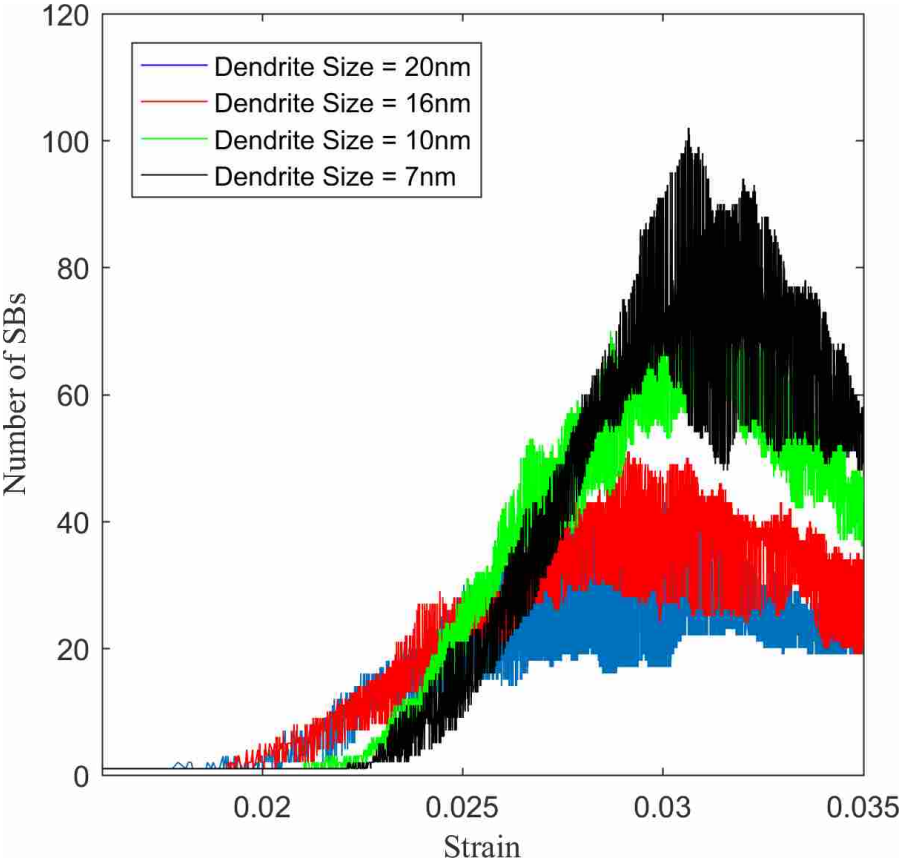

Figure 3-19: The number of shear bands during straining of each simulation.
All 6 simulations for each dendrite size is plotted together as one large data set.

3.5.2.3 Shear band propagation

There are numerous ways in which shear bands interact with dendrites [75]. Smaller dendrites are more prone to participate in shear banding as shear bands are able to propagate through the dendrite. Larger dendrites tend to act as a barrier and shore up strain accumulation at the dendrite-matrix interface. This is shown by the plot in Figure 3-20. This plot shows for 4 example simulations the degree of participation by the crystalline phase in shear banding over

time. This figure shows that simulations with smaller dendrites on average saw a larger participation in shear banding by the crystalline phase. This can have three repercussions: 1) ductility is enhanced as the crystalline phase is accommodating more strain, 2) crack initiation is either delayed or discouraged from happening in the metallic glass phase as there is less overall strain in the metallic glass matrix, and 3) shear bands propagate slowly through crystalline dendrites resulting in shear bands not being able to relax the specimen sufficiently fast enough which encourages strain accumulation in other shear bands.

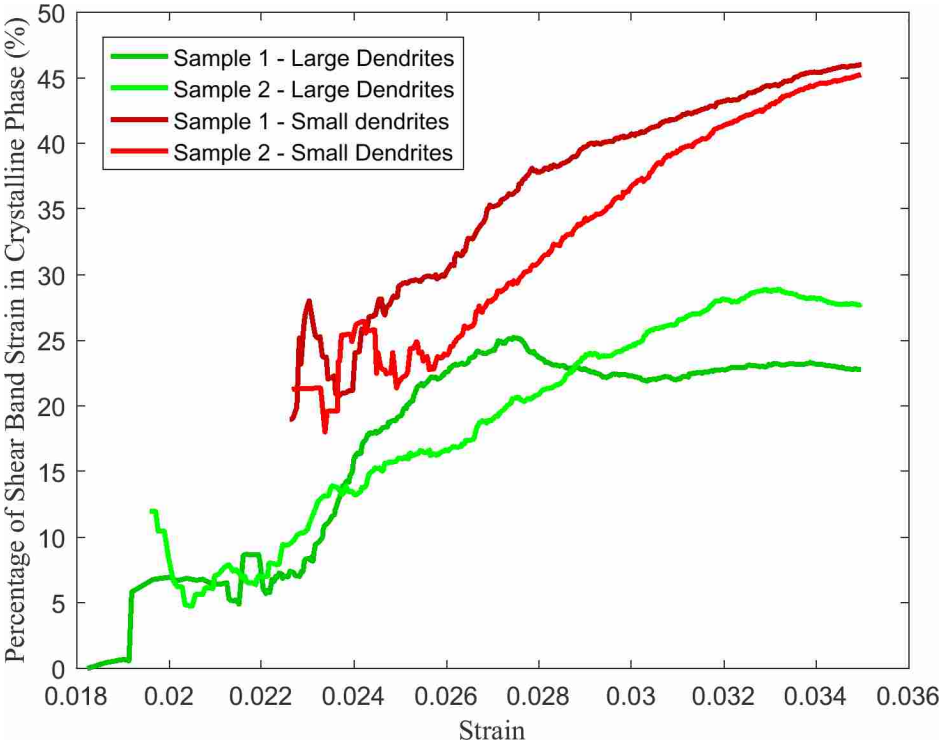

Figure 3-20: Percentage of shear band strain carried by the crystalline phase
2 large (20nm) and 2 small (7nm) example simulations (red – small, green – large) are shown.

On the other hand, simulations with large dendrites will tend to stop a shear band at the boundary between dendrite and glass matrix. Interestingly, this is less desirable than having the shear band propagate through the dendrite. This is because shear bands that grow through a dendrite will dissipate stress concentrations better than shear bands piling up at the interface.

Eventually, enough stress will accumulate that will then propagate the shear band very quickly through the dendrite resulting in a run-away shear band. In this sense, smaller dendrites are more desirable as more of the crystalline phase participates in shear banding earlier in the simulation.

3.6 Summary

MGMCs were modelled numerically using STZ dynamics. The dendrite sizes were systematically varied between 4 different dendrite sizes. Analysis of shear banding characteristics yielded evidence of a competition of shear band nucleation and propagation rates previously seen only in metallic glasses strained at high rates. Increased strain delocalization as a result of a competition of rates was seen to occur at smaller dendrite sizes.

4 CONCLUSIONS

4.1 Combined simulated-experimental nanoindentation and verification of individual phase material properties

Indentation of phases of varying thickness was carried out numerically. Results were normalized and compared with nanoindentation experiments. The following length scales were discovered:

1) An indenter displacement less than 10% of the average dendrite size is needed to accurately capture the crystalline phase elastic modulus.
2) An indenter displacement less than 50% of the average dendrite size is needed to accurately capture the crystalline phase hardness.
3) An indenter displacement less than 20% of the average dendrite spacing is needed to accurately capture the amorphous phase elastic modulus.
4) An indenter displacement less than 30% of the average dendrite spacing is needed to accurately capture the amorphous phase hardness.

Material properties as measured from a combined simulated-experimental approach was reported and found to be consistent with other literature. Numerical and experimental material properties are in agreement with each other and verifies the material properties reported here.

4.2 Competition of rates in MGMCs

The present work provides new insight into the mechanisms behind strain delocalization in MGMCs. This mechanism is investigated using systematic variation of life-like dendritic structures in MGMCs using STZ dynamics. This allows examination time and length scales intermediate to atomistic and continuum methods. Both macroscopic and microscopic characterizations are analyzed and discussed. Dendrite sizes and spacings examined spanned 7-20nm and 17-50nm respectively while volume fraction was held constant at ~64.5%. Images of DH3 MGMC specimens were used to create the dendritic structure. Material inputs determined from a combined simulated-experimental nanoindentation approach were used in this model

Statistical analysis of shear banding characteristics supports the hypothesis that the competition of shear band nucleation and propagation rates is the underlying mechanism encouraging strain delocalization in MGMCs. By introducing a crystalline dendritic structure into the amorphous matrix, a greater number of shear bands are encouraged to nucleate. At the same time, the crystalline dendrites also reduce the propagation or growth rates of shear bands.

It was demonstrated that decreasing dendrite sizes yielded greater strain delocalization among more shear bands. It was also found that at these smaller microstructural sizes, the onset of run-away shear bands was delayed and overall growth rates were lower. These smaller dendrites allowed greater strain delocalization by allowing a greater fraction of the crystalline phase to participate in the shear banding process.

These findings suggest a particular approach to utilize in the creation of less brittle MGMCs. In order to encourage more homogenous deformation, the goal is to distribute plastic strain over as many shear bands as possible. This results in a two-fold approach: 1) encourage as

large a number of shear band nucleation events as possible and 2) reduce the propensity for shear bands to propagate. This can be done to a greater degree using smaller dendrites oriented randomly throughout the matrix. This allows a larger number of stress concentrations encouraging diverse shear band nucleation early on in the simulation. Small dendrites can then participate in shear banding which reduces their propagation rates. This in turn encourages greater shear band nucleation events to help relax the system as shear bands are not growing fast enough to do so.

These results are consistent with findings in experimental work while clarifying the mechanics underpinning what is seen.

4.3 Future work

Results demonstrated here would be strengthened with the following recommended work:

- Smooth dendrite-matrix interfaces: elements are triangular in nature and results in a somewhat jagged interface. This can cause stress concentrations not seen in experiment.
- Failure mode for the crystalline phase: incorporating a failure mode would allow a real examination on the effects of microstructure on MGMC tensile strengths. It would also remove potential hardening effects that might be occurring (see Figure 3-20).
- N-factorial analysis on the effects of different microstructural characteristics: this would allow us to capture the extent and isolate the effects of different microstructural characteristics.

- Extend dendritic mimicry to 3D: the current simulation utilizes plane strain elements which assumes an infinitely thick specimen.

REFERENCES

[1] W. KLEMENT, R. H. WILLENS, and P. O. L. DUWEZ, "Non-crystalline Structure in Solidified Gold-Silicon Alloys," *Nature*, vol. 187, no. 4740, pp. 869–870, Sep. 1960.

[2] A. Peker and W. L. Johnson, "A highly processable metallic glass: Zr41.2Ti13.8Cu12.5Ni10.0Be22.5," *Appl. Phys. Lett.*, vol. 63, no. 17, pp. 2342–2344, 1993.

[3] A. Inoue, T. Zhang, and T. Masumoto, "Zr-Al-Ni Amorphous Alloys with High Glass Transition Temperature and Significant Supercooled Liquid Region," *Materials Transactions, JIM*, vol. 31, no. 3. pp. 177–183, 1990.

[4] A. Inoue, N. Nishiyama, K. Amiya, T. Zhang, and T. Masumoto, "Ti-based amorphous alloys with a wide supercooled liquid region," *Mater. Lett.*, vol. 30, no. 12, pp. 965–972, May 1989.

[5] A. Inoue, K. Ohtera, K. Kita, and T. Masumoto, "New amorphous Mg-Ce-Ni alloys with high strength and good ductility," *Japanese J. Appl. Physics, Part 1 Regul. Pap. Short Notes Rev. Pap.*, vol. 27, no. 12, pp. 2248–2251, 1988.

[6] H. A. Bruck, T. Christman, A. J. Rosakis, and W. L. Johnson, "Quasi-static constitutive behavior of Zr41.25Ti13.75Ni10Cu12.5Be22.5 bulk amorphous alloys," *Scr. Metall. Mater.*, vol. 30, no. 4, pp. 429–434, 1994.

[7] H. A. Bruck, A. J. Rosakis, and W. L. Johnson, "The dynamic compressive behavior of beryllium bearing bulk metallic glasses," *J. Mater. Res.*, vol. 11, no. 02, pp. 503–511, Jan. 1996.

[8] G. Subhash, R. J. Dowding, and L. J. Kecskes, "Characterization of uniaxial compressive response of bulk amorphous Zr-Ti-Cu-Ni-Be alloy," *Mater. Sci. Eng. A*, vol. 334, no. 1–2, pp. 33–40, 2002.

[9] M. Telford, "The case for bulk metallic glass," *Mater. Today*, vol. 7, no. 3, pp. 36–43, 2004.

[10] A. L. Greer, "Metallic glasses...on the threshold," *Mater. Today*, vol. 12, no. 1–2, pp. 14–22, 2009.

[11] W. H. Wang, C. Dong, and C. H. Shek, "Bulk metallic glasses," *Mater. Sci. Eng. R Reports*, vol. 44, no. 2–3, pp. 45–90, 2004.

[12] E. R. Homer, M. B. Harris, S. A. Zirbel, J. A. Kolodziejska, H. Kozachkov, B. P. Trease, J. P. C. Borgonia, G. S. Agnes, L. L. Howell, and D. C. Hofmann, "New methods for developing and manufacturing compliant mechanisms utilizing bulk metallic glass," *Adv. Eng. Mater.*, vol. 16, no. 7, pp. 850–856, 2014.

[13] A. Peker and W. L. Johnson, "A highly processable metallic glass: Zr41.2Ti13.8Cu12.5Ni10.0Be22.5," vol. 63, no. 17, pp. 2342–2345, 1993.

[14] C. SCHUH, T. HUFNAGEL, and U. RAMAMURTY, "Mechanical behavior of amorphous alloys," *Acta Mater.*, vol. 55, no. 12, pp. 4067–4109, 2007.

[15] A. S. Argon, “Plastic deformation in metallic glasses,” *Acta Metall.*, vol. 27, no. 1, pp. 47–58, 1979.

[16] A. S. Argon and H. Y. Kuo, “Plastic flow in a disordered bubble raft (an analog of a metallic glass),” *Mater. Sci. Eng.*, vol. 39, no. 1, pp. 101–109, 1979.

[17] A. S. Argon, “Inelastic Deformation and Fracture of Glassy Solids,” in *Materials Science and Technology*, Wiley-VCH Verlag GmbH & Co. KGaA, 2006.

[18] T. C. Hufnagel, T. Jiao, Y. Li, L.-Q. Xing, and K. T. Ramesh, “Glass Under Quasi-Static and Dynamic Compression,” *J. Mater. Res.*, vol. 17, no. 6, pp. 1441–1445, 2002.

[19] H. Neuhäuser, “Rate of shear band formation in metallic glasses. Scripta Metall 1978;12:471–4.” .

[20] W. J. Wright, M. W. Samale, T. C. Hufnagel, M. M. LeBlanc, and J. N. Florando, “Studies of shear band velocity using spatially and temporally resolved measurements of strain during quasistatic compression of a bulk metallic glass,” *Acta Mater.*, vol. 57, no. 16, pp. 4639–4648, Sep. 2009.

[21] S. X. Song, X.-L. Wang, and T. G. Nieh, “Capturing shear band propagation in a Zr-based metallic glass using a high-speed camera,” *Scr. Mater.*, vol. 62, no. 11, pp. 847–850, Jun. 2010.

[22] E. R. Homer and C. A. Schuh, “Mesoscale modeling of amorphous metals by shear transformation zone dynamics,” *Acta Mater.*, vol. 57, no. 9, pp. 2823–2833, 2009.

[23] J. J. Kruzic, “Bulk Metallic Glasses as Structural Materials: A Review,” *Adv. Eng. Mater.*, no. 8, 2016.

[24] A. L. Greer, Y. Q. Cheng, and E. Ma, “Shear bands in metallic glasses,” *Mater. Sci. Eng. R Reports*, vol. 74, no. 4, pp. 71–132, 2013.

[25] T. Mukai, T. G. Nieh, Y. Kawamura, A. Inoue, and K. Higashi, “Effect of strain rate on compressive behavior of a Pd 40 Ni 40 P 20 bulk metallic glass,” *Intermetallics*, vol. 10, pp. 1071–1077, 2002.

[26] A. V. Sergueeva, N. A. Mara, D. J. Branagan, and A. K. Mukherjee, “Strain rate effect on metallic glass ductility,” *Scr. Mater.*, vol. 50, no. 10, pp. 1303–1307, 2004.

[27] A. V. Sergueeva, N. A. Mara, J. D. Kuntz, D. J. Branagan, and A. K. Mukherjee, “Shear band formation and ductility of metallic glasses,” *Mater. Sci. Eng. A*, vol. 383, no. 2, pp. 219–223, 2004.

[28] F. H. Dalla Torre, A. Dubach, A. Nelson, and J. F. Löffler, “Temperature, Strain and Strain Rate Dependence of Serrated Flow in Bulk Metallic Glasses,” *Mater. Trans.*, vol. 48, no. 7, pp. 1774–1780, 2007.

[29] A. Dubach, F. H. Dalla Torre, and J. F. Löffler, “Deformation kinetics in Zr-based bulk metallic glasses and its dependence on temperature and strain-rate sensitivity,” *Philos. Mag. Lett.*, vol. 87, no. 9, pp. 695–704, 2007.

[30] A. Beu, P. Colloque, B. B. Moser, J. Kuebler, H. Meinhard, W. Muster, and J. Michler, "Observation of Instabilities during Plastic Deformation by in-situ SEM Indentation Experiments," no. 5, pp. 388–392, 2005.

[31] A. L. Greer and I. T. Walker, "Transformations in Primary Crystallites in (Fe,Ni)-Based Metallic Glasses," in *Metastable, Mechanically Alloyed and Nanocrystalline Materials 2001*, 2002, vol. 386, pp. 77–88.

[32] W. J. Wright, R. Saha, and W. D. Nix, "Deformation mechanisms of the Zr40Ti14Ni10Cu12Be24 bulk metallic glass," *Mater. Trans.*, vol. 42, no. 4, pp. 642–649, 2001.

[33] Y. I. Golovin, V. I. Ivolgin, V. a Khonik, and K. Kitagawa, "Serrated plastic ¯ ow during nanoindentation of a bulk metallic glass," *Scr. Mater.*, vol. 45, no. 8, pp. 947–952, 2001.

[34] J. H. Perepezko, S. D. Imhoff, M.-W. Chen, J.-Q. Wang, and S. Gonzalez, "Nucleation of shear bands in amorphous alloys," *Proc. Natl. Acad. Sci.*, vol. 111, no. 11, pp. 3938–3942, 2014.

[35] C. A. Schuh, A. C. Lund, and T. G. Nieh, "New regime of homogeneous flow in the deformation map of metallic glasses: elevated temperature nanoindentation experiments and mechanistic modeling," *Acta Mater.*, vol. 52, no. 20, pp. 5879–5891, 2004.

[36] C. a. Schuh, a. S. Argon, T. G. Nieh, and J. Wadsworth, "The transition from localized to homogeneous plasticity during nanoindentation of an amorphous metal," *Philos. Mag.*, vol. 83, no. August, pp. 2585–2597, 2003.

[37] C. A. Schuh, T. G. Nieh, and Y. Kawamura, "Rate Dependence of Serrated Flow During Nanoindentation of a Bulk Metallic Glass," *J. Mater. Res.*, vol. 17, no. 7, pp. 1651–1654, 2002.

[38] T. G. Nieh, C. Schuh, J. Wadsworth, and Y. Li, "Strain rate-dependent deformation in bulk metallic glasses," *Intermetallics*, vol. 10, no. 11–12, pp. 1177–1182, 2002.

[39] M. B. Harris, L. S. Watts, and E. R. Homer, "Competition between shear band nucleation and propagation across rate-dependent flow transitions in a model metallic glass," *Acta Mater.*, vol. 111, pp. 273–282, Jun. 2016.

[40] J. P. Schramm, D. C. Hofmann, M. D. Demetriou, and W. L. Johnson, "Metallic-glass-matrix composite structures with benchmark mechanical performance," *Appl. Phys. Lett.*, vol. 97, no. 24, 2010.

[41] F. Szuecs, C. P. Kim, and W. L. Johnson, "Mechanical properties of Zr56.2Ti13.8Nb5.0Cu6.9Ni5.6Be12.5 ductile phase reinforced bulk metallic glass composite," *Acta Mater.*, vol. 49, no. 9, pp. 1507–1513, May 2001.

[42] C. C. Hays, C. P. Kim, and W. L. Johnson, "Microstructure controlled shear band pattern formation and enhanced plasticity of bulk metallic glasses containing in situ formed ductile phase dendrite dispersions," *Phys. Rev. Lett.*, vol. 84, no. 13, pp. 2901–2904, 2000.

[43] J. W. Qiao, H. Y. Ye, Y. S. Wang, S. Pauly, H. J. Yang, and Z. H. Wang, "Distinguished work-hardening capacity of a Ti-based metallic glass matrix composite upon dynamic

loading," *Mater. Sci. Eng. A*, vol. 585, pp. 277–280, 2013.

[44] R. L. Narayan, P. S. Singh, D. C. Hofmann, N. Hutchinson, K. M. Flores, and U. Ramamurty, "On the microstructure–tensile property correlations in bulk metallic glass matrix composites with crystalline dendrites," *Acta Mater.*, vol. 60, no. 13–14, pp. 5089–5100, 2012.

[45] H. Choi-Yim and W. L. Johnson, "Bulk metallic glass matrix composites," *Appl. Phys. Lett.*, vol. 71, no. 26, pp. 3808–3810, 1997.

[46] D. C. Hofmann, J.-Y. Suh, A. Wiest, G. Duan, M.-L. Lind, M. D. Demetriou, and W. L. Johnson, "Designing metallic glass matrix composites with high toughness and tensile ductility," *Nature*, vol. 451, no. 7182, pp. 1085–1089, 2008.

[47] X. L. Fu, Y. Li, and C. A. Schuh, "Mechanical properties of metallic glass matrix composites: Effects of reinforcement character and connectivity," *Scr. Mater.*, vol. 56, no. 7, pp. 617–620, Apr. 2007.

[48] J. W. Qiao, S. Wang, Y. Zhang, P. K. Liaw, and G. L. Chen, "Large plasticity and tensile necking of Zr-based bulk-metallic-glass-matrix composites synthesized by the Bridgman solidification," *Appl. Phys. Lett.*, vol. 94, no. 15, pp. 2007–2010, 2009.

[49] J. Qiao, H. Jia, and P. K. Liaw, "Metallic glass matrix composites," *Mater. Sci. Eng. R Reports*, vol. 100, pp. 1–69, 2016.

[50] J. Eckert, J. Das, S. Pauly, and C. Duhamel, "Mechanical properties of bulk metallic glasses and composites," *J. Mater. Res.*, vol. 22, no. 02, pp. 285–301, 2007.

[51] J. W. Qiao, J. T. Zhang, F. Jiang, Y. Zhang, P. K. Liaw, Y. Ren, and G. L. Chen, "Development of plastic Ti-based bulk-metallic-glass-matrix composites by controlling the microstructures," *Mater. Sci. Eng. A*, vol. 527, no. 29–30, pp. 7752–7756, 2010.

[52] J. W. Qiao, A. C. Sun, E. W. Huang, Y. Zhang, P. K. Liaw, and C. P. Chuang, "Tensile deformation micromechanisms for bulk metallic glass matrix composites: From work-hardening to softening," *Acta Mater.*, vol. 59, no. 10, pp. 4126–4137, 2011.

[53] D. C. Hofmann, "Designing Bulk Metallic Glass Matrix Composites with High Toughness and Tensile Ductility," vol. 2009, p. 201, 2009.

[54] C. C. Hays, W. L. Johnson, and C. N. P. Kim, "Enhanced Plasticity of Bulk Metallic Glasses Containing Ductile Phase Dendrite Dispersions," in *Metastable, Mechanically Alloyed and Nanocrystalline Materials 1999*, 2000, vol. 343, pp. 191–196.

[55] J. Gao, J. Sharp, D. Guan, W. M. Rainforth, and I. Todd, "New compositional design for creating tough metallic glass composites with excellent work hardening," *Acta Mater.*, vol. 86, pp. 208–215, 2015.

[56] W. Zhang, A. J. Bodey, T. Sui, W. Kockelmann, C. Rau, A. M. Korsunsky, and J. Mi, "Multi-scale Characterisation of the 3D Microstructure of a Thermally-Shocked Bulk Metallic Glass Matrix Composite," *Sci. Rep.*, vol. 6, no. October 2015, p. 18545, 2016.

[57] D. C. Hofmann, "Bulk Metallic Glasses and Their Composites: A Brief History of

Diverging Fields," *J. Mater.*, vol. 2013, p. e517904, 2013.

[58] J. Eckert, J. Das, S. Pauly, and C. Duhamel, "Processing Routes, Microstructure and Mechanical Properties of Metallic Glasses and their Composites," *Adv. Eng. Mater.*, vol. 9, no. 6, pp. 443–453, 2007.

[59] F. Abdeljawad, M. Fontus, and M. Haataja, "Ductility of bulk metallic glass composites: Microstructural effects," *Appl. Phys. Lett.*, vol. 98, no. 3, pp. 1–4, 2011.

[60] M. L. Lee, Y. Li, and C. A. Schuh, "Effect of a controlled volume fraction of dendritic phases on tensile and compressive ductility in La-based metallic glass matrix composites," *Acta Mater.*, vol. 52, no. 14, pp. 4121–4131, 2004.

[61] Y. Zhang, W. Xu, H. Tan, and Y. Li, "Microstructure control and ductility improvement of La-Al-(Cu, Ni) composites by Bridgman solidification," *Acta Mater.*, vol. 53, no. 9, pp. 2607–2616, 2005.

[62] S. Pauly, J. Das, J. Bednarcik, N. Mattern, K. B. Kim, D. H. Kim, and J. Eckert, "Deformation-induced martensitic transformation in Cu-Zr-(Al,Ti) bulk metallic glass composites," *Scr. Mater.*, vol. 60, no. 6, pp. 431–434, 2009.

[63] D. C. Hofmann, J.-Y. Suh, A. Wiest, M.-L. Lind, M. D. Demetriou, and W. L. Johnson, "Development of tough, low-density titanium-based bulk metallic glass matrix composites with tensile ductility," *Proc. Natl. Acad. Sci.*, vol. 105, no. 51, pp. 20136–20140, 2008.

[64] X. L. Fu, Y. Li, and C. A. Schuh, "Temperature, strain rate and reinforcement volume fraction dependence of plastic deformation in metallic glass matrix composites," *Acta Mater.*, vol. 55, no. 9, pp. 3059–3071, 2007.

[65] J. C. Lee, Y. C. Kim, J. P. Ahn, and H. S. Kim, "Enhanced plasticity in a bulk amorphous matrix composite: Macroscopic and microscopic viewpoint studies," *Acta Mater.*, vol. 53, no. 1, pp. 129–139, 2005.

[66] M. E. Launey, D. C. Hofmann, J. Y. Suh, H. Kozachkov, W. L. Johnson, and R. O. Ritchie, "Fracture toughness and crack-resistance curve behavior in metallic glass-matrix composites," *Appl. Phys. Lett.*, vol. 94, pp. 2009–2011, 2009.

[67] J. L. Cheng, G. Chen, F. Xu, Y. L. Du, Y. S. Li, and C. T. Liu, "Correlation of the microstructure and mechanical properties of Zr-based in-situ bulk metallic glass matrix composites," *Intermetallics*, vol. 18, no. 12, pp. 2425–2430, 2010.

[68] T. Zhang, H. Y. Ye, J. Y. Shi, H. J. Yang, and J. W. Qiao, "Dendrite size dependence of tensile plasticity of in situ Ti-based metallic glass matrix composites," *J. Alloys Compd.*, vol. 583, pp. 593–597, 2014.

[69] S. H. Hong, J. T. Kim, M. W. Lee, J. M. Park, M. H. Lee, B. S. Kim, J. Y. Park, Y. Seo, J. Y. Suh, P. Yu, M. Qian, and K. B. Kim, "Combinatorial influence of bimodal size of B2 TiCu compounds on plasticity of Ti-Cu-Ni-Zr-Sn-Si bulk metallic glass composites," *Metall. Mater. Trans. A Phys. Metall. Mater. Sci.*, vol. 45, no. 5, pp. 2376–2381, 2014.

[70] T. C. Hufnagel, T. Jiao, Y. Li, L.-Q. Xing, and K. T. Ramesh, "Deformation and Failure of Zr57Ti5Cu20Ni8Al10 Bulk Metallic Glass Under Quasi-static and Dynamic

Compression," *J. Mater. Res.*, vol. 17, no. 6, pp. 1441–1445, 2002.

[71] P. E. Donovan and W. M. Stobbs, "The structure of shear bands in metallic glasses," *Acta Metall.*, vol. 29, no. 8, pp. 1419–1436, Aug. 1981.

[72] E. Pekarskaya, C. P. Kim, and W. L. Johnson, "In situ transmission electron microscopy studies of shear bands in a bulk metallic glass based composite," *J. Mater. Res.*, vol. 16, no. 9, pp. 2513–2518, 2001.

[73] M. Zink, K. Samwer, W. L. Johnson, and S. G. Mayr, "Plastic deformation of metallic glasses: Size of shear transformation zones from molecular dynamics simulations," *Phys. Rev. B - Condens. Matter Mater. Phys.*, vol. 73, no. 17, pp. 2–4, 2006.

[74] C. E. Packard, E. R. Homer, N. Al-Aqeeli, and C. a. Schuh, "Cyclic hardening of metallic glasses under Hertzian contacts: Experiments and STZ dynamics simulations," *Philos. Mag.*, vol. 90, no. 10, pp. 1373–1390, 2010.

[75] T. J. Hardin and E. R. Homer, "Microstructural factors of strain delocalization in model metallic glass matrix composites," *Acta Mater.*, vol. 83, pp. 203–215, 2015.

[76] D. Tabor, *The hardness of metals.* Oxford: Clarendon Press, 1951.

[77] D. Tabor, "The Hardness of Solids," *Rev. Phys. Technol.*, vol. 1, no. 3, pp. 145–179, 1970.

[78] M. F. Doerner and W. D. Nix, "A method for interpreting the data from depth-sensing indentation instruments," *J. Mater. Res.*, vol. 1, no. 4, pp. 601–609, 1986.

[79] W. . Oliver and G. . Pharr, "An improved technique for determing hardness and elastic modulus using load and displacement sensing indentation experiments," *J. Mater. Res.*, vol. 7, no. 6, 1992.

[80] W. . Oliver and G. . Pharr, "Measurement of hardness and elastic modulus by instrumented indentation Advances in understanding and refinements to methodology," *Mater. Res. Soc.*, vol. 19, no. 1, pp. 3–20, 2004.

[81] G. M. Pharr, "Measurement of mechanical properties by ultra-low load indentation," *Mater. Sci. Eng. A*, vol. 253, no. 1–2, pp. 151–159, 1998.

[82] M. J. Bamber, K. E. Cooke, A. B. Mann, and B. Derby, "Accurate determination of Young's modulus and Poisson's ratio of thin films by a combination of acoustic microscopy and nanoindentation," *Thin Solid Films*, vol. 398–399, pp. 299–305, 2001.

[83] G. M. Pharr, E. G. Herbert, and Y. Gao, "The Indentation Size Effect: A Critical Examination of Experimental Observations and Mechanistic Interpretations," *Annu. Rev. Mater. Res.*, vol. 40, no. 1, pp. 271–292, 2010.

[84] A. W. Warren and Y. B. Guo, "Machined surface properties determined by nanoindentation: Experimental and FEA studies on the effects of surface integrity and tip geometry," *Surf. Coatings Technol.*, vol. 201, no. 1–2, pp. 423–433, 2006.

[85] S. W. Moore, M. T. Manzari, and Y.-L. Shen, "Nanoindentation in elastoplastic materials: insights from numerical simulations."

[86] K. Durst, M. Göken, and H. Vehoff, “Finite element study for nanoindentation measurements on two-phase materials,” *J. Mater. Res.*, vol. 19, no. JANUARY 2004, pp. 85–93, 2004.

[87] J. D. Bressan, A. Tramontin, and C. Rosa, “Modeling of nanoindentation of bulk and thin film by finite element method,” *Wear*, vol. 258, no. 1–4 SPEC. ISS., pp. 115–122, 2005.

[88] B. D. Kozola and Y. L. Shen, “A mechanistic analysis of the correlation between overall strength and indentation hardness in discontinuously reinforced aluminum,” *J. Mater. Sci.*, vol. 38, no. 5, pp. 901–907, 2003.

[89] H. S. Kim, M. B. Bush, and Y. Estrin, “A phase mixture model of a particle reinforced composite with fine microstructure,” *Mater. Sci. Eng. A*, vol. 276, no. 1–2, pp. 175–185, 2000.

[90] M. Rodríguez, J. M. Molina-Aldareguía, C. González, and J. LLorca, “Determination of the mechanical properties of amorphous materials through instrumented nanoindentation,” *Acta Mater.*, vol. 60, no. 9, pp. 3953–3964, 2012.

[91] W. Yan, C. L. Pun, Z. Wu, and G. P. Simon, “Some issues on nanoindentation method to measure the elastic modulus of particles in composites,” *Compos. Part B Eng.*, vol. 42, no. 8, pp. 2093–2097, 2011.

[92] W. Yan, C. L. Pun, and G. P. Simon, “Conditions of applying Oliver-Pharr method to the nanoindentation of particles in composites,” *Compos. Sci. Technol.*, vol. 72, no. 10, pp. 1147–1152, 2012.

[93] N. Panich, V. Kraivichien, and S. Yong, “Finite Element Simulation of Nanoindentation of Bulk Materials,” *J. Sci. Res.*, vol. 29, no. 2, pp. 145–153, 2004.

[94] M. Lichinchi, C. Lenardi, J. Haupt, and R. Vitali, “Simulation of Berkovich nanoindentation experiments on thin films using finite element method,” *Thin Solid Films*, vol. 312, no. 1–2, pp. 240–248, 1998.

[95] A. Grill, “Review of the tribology of diamond-like carbon,” *Wear*, vol. 168, no. 1–2, pp. 143–153, 1993.

[96] A. Clausner and F. Richter, “Determination of yield stress from nano-indentation experiments,” *Eur. J. Mech. - A/Solids*, vol. 51, pp. 11–20, 2015.

[97] S. G. Ma, Z. M. Jiao, J. W. Qiao, H. J. Yang, Y. Zhang, and Z. H. Wang, “Strain rate effects on the dynamic mechanical properties of the AlCrCuFeNi2 high-entropy alloy,” *Mater. Sci. Eng. A*, vol. 649, no. September, pp. 35–38, 2016.

[98] R. T. Qu, Z. Q. Liu, R. F. Wang, and Z. F. Zhang, “Yield strength and yield strain of metallic glasses and their correlations with glass transition temperature,” *J. Alloys Compd.*, vol. 637, pp. 44–54, 2015.

[99] J. Eckert, J. Das, G. He, M. Calin, and K. B. Kim, “Ti-base bulk nanostructure-dendrite composites: Microstructure and deformation,” *Mater. Sci. Eng. A*, vol. 448–451, no. August 2014, pp. 24–29, 2007.

[100] J. H. Chen, M. Q. Jiang, Y. Chen, and L. H. Dai, “Strain rate dependent shear banding behavior of a Zr-based bulk metallic glass composite,” *Mater. Sci. Eng. A*, vol. 576, pp. 134–139, 2013.

[101] Y. S. Wang, G. J. Hao, J. W. Qiao, Y. Zhang, and J. P. Lin, “High strain rate compressive behavior of Ti-based metallic glass matrix composites,” *Intermetallics*, vol. 52, pp. 138–143, 2014.

[102] M. Martin, L. Kecskes, and N. N. Thadhani, “High-strain-rate dynamic mechanical behavior of a bulk metallic glass composite,” *J. Mater. Res.*, vol. 23, no. 4, pp. 998–1008, 2008.

[103] A. J. Zaddach, R. O. Scattergood, and C. C. Koch, “Tensile properties of low-stacking fault energy high-entropy alloys,” *Mater. Sci. Eng. A*, vol. 636, pp. 373–378, 2015.

[104] E. R. Homer, “Modeling the Mechanical Behavior of Amorphous Metals by Shear Transformation Zone Dynamics,” 2010.

[105] E. R. Homer, D. Rodney, and C. a. Schuh, “Kinetic Monte Carlo study of activated states and correlated shear-transformation-zone activity during the deformation of an amorphous metal,” *Phys. Rev. B - Condens. Matter Mater. Phys.*, vol. 81, pp. 1–11, 2010.

[106] D. T. Fullwood, S. R. Niezgoda, and S. R. Kalidindi, “Microstructure reconstructions from 2-point statistics using phase-recovery algorithms,” *Acta Mater.*, vol. 56, no. 5, pp. 942–948, 2008.

[107] D. T. Fullwood, S. R. Niezgoda, B. L. Adams, and S. R. Kalidindi, “Microstructure sensitive design for performance optimization,” *Prog. Mater. Sci.*, vol. 55, no. 6, pp. 477–562, 2010.

[108] Q. K. Li and M. Li, “Assessing the critical sizes for shear band formation in metallic glasses from molecular dynamics simulation,” *Appl. Phys. Lett.*, vol. 91, no. 23, pp. 89–92, 2007.

[109] C. E. Packard and C. A. Schuh, “Initiation of shear bands near a stress concentration in metallic glass,” *Acta Mater.*, vol. 55, no. 16, pp. 5348–5358, 2007.

[110] E. R. Homer, “Examining the initial stages of shear localization in amorphous metals,” *Acta Mater.*, vol. 63, pp. 44–53, 2014.